Bioactive Materials 25 (2023) 748–765

Contents lists available at ScienceDirect

Bioactive Materials

journal homepage: www.keaipublishing.com/en/journals/bioactive-materials

Rapid sterilisation and diabetic cutaneous regeneration using cascade bio-heterojunctions through glucose oxidase-primed therapy

Yi Deng [a,b,g,1], Xumei Ouyang [c,1], Jiyu Sun [d], Xiuyuan Shi [e], Yunfei Li [f], Yau Kei Chan [h], Weizhong Yang [a,*], Shaojun Peng [c,**]

[a] College of Biomedical Engineering, School of Chemical Engineering, Sichuan University, Chengdu, 610065, China
[b] State Key Laboratory of Polymer Materials Engineering, Sichuan University, Chengdu, 610065, China
[c] Zhuhai Institute of Translational Medicine, Zhuhai People's Hospital (Zhuhai Hospital Affiliated with Jinan University), Zhuhai, Guangdong, 519000, China
[d] State Key Laboratory of Oral Diseases, National Clinical Research Center for Oral Diseases, West China Hospital of Stomatology, Sichuan University, Chengdu, 610041, China
[e] Department of Materials, Imperial College London, SW7 2AZ, London, United Kingdom
[f] Department of Biomedical Engineering, The City College of the City University of New York, New York, United States
[g] Department of Mechanical Engineering, The University of Hong Kong, Hong Kong, China
[h] Department of Ophthalmology, The University of Hong Kong, Hong Kong, China

ARTICLE INFO

Keywords:
Antibacterial therapy
Bio-heterojunction
g-C_3N_4
Rapid sterilization
Tissue regeneration

ABSTRACT

The cutaneous wound in diabetic patients frequently encounters intractable pathogenic infections due to the hyperglycemia micromilieu which is conducive to bacterial growth and multiplication. Despite the extensive clinical use of antibiotics to treat bacterial infections, the emergence of drug-resistant and super pathogens as well as the potential side effects of antibiotics have elicited alarming challenges to public health. To address this daunting concern, we devise and develop a photo-activated cascade bio-heterojunctions (C-bio-HJs) for rapid sterilization and diabetic cutaneous regeneration. In the designed C-bio-HJs, photo-generated electron-hole pairs of graphite-phase carbon nitride (g-C_3N_4) are effectively separated with the marriage of molybdenum disulfide (MoS_2), which achieves the augmented photodynamic antibacterial effect. Moreover, glucose oxidase (GOx) tethered on the bio-HJs catalyzes glucose into hydrogen peroxide (H_2O_2) in diabetic wounds for starvation therapy. Furthermore, Mo^{4+} enables the catalysis of H_2O_2 into a highly effective hydroxyl radical (·OH) for chemodynamic-photothermal combined antibacterial therapy. Both *in vitro* and *in vivo* results authenticate the cascading antibacterial properties and skin regeneration-promoting effects of the C-bio-HJs, which provide a facile strategy to combat diabetic wound healing through the synergistic GOx-primed dynamic therapies.

1. Introduction

The wound healing process is frequently accompanied by pathogenic infections, especially in diabetic patients [1–3]. As the chronic state of hyperglycemia provides a breeding ground for bacteria, the skin wound in diabetic patients becomes difficult to heal and more susceptible to bacterial infections [4,5]. Furthermore, the clinical abuse of antibiotics has led to the emergence of drug-resistant bacteria and superbugs, making bacterial infections a serious threat to human health, especially for patients with chronic diseases [6,7]. As bacterial resistance develops, new antibiotics are desperately needed, whereas the time required to develop a new antibiotic far outweighs the time required to develop antibiotic resistance. In addition, small-molecule antibiotics could cause certain detrimental reactions and damage to the normal tissues [8]. Therefore, there is a pressing necessity to develop novel therapeutic methods to combat bacterial infections and drug resistance.

In recent years, numerous advanced nanomaterials have been developed, which demonstrated great potential in disease treatment [9,10]. For instance, Dong et al. developed mesoporous silica supported silver-bismuth nanoparticles, which exhibited excellent performance

Peer review under responsibility of KeAi Communications Co., Ltd.
* Corresponding author.
** Corresponding author.
E-mail addresses: ywz@scu.edu.cn (W. Yang), shaojunpeng@ext.jnu.edu.cn (S. Peng).
[1] Y. Deng and X. Ouyang contributed equally to this work.

https://doi.org/10.1016/j.bioactmat.2022.07.003
Received 30 April 2022; Received in revised form 21 June 2022; Accepted 2 July 2022
Available online 31 July 2022

against drug-resistant bacteria [11]. In addition, Zhang et al. fabricated metal-organic frame nanoparticles with superior mechanical strength and interconnected pore support structure for the treatment of bone tissue repair engineering [12]. Based on the development of functional nanomaterials, many effective novel antibacterial therapeutic strategies have been exploited, including phototherapy, chemodynamic therapy (CDT), sonodynamic therapy (SDT), microwave therapy (MWT), and ion therapy [13–15]. Among these, phototherapy that contains photothermal therapy (PTT) and photodynamic therapy (PDT) has garnered ever-increasing attention as a highly promising remedial strategy with unique antibacterial features such as flexibility and controllability, rapidity, efficiency, and safety [16–18]. During near-infrared (NIR) irradiation, photothermal converters can produce hyperthermia to interfere with metabolism and damage DNA in the organism and photocatalyst causes bacterial damage by utilizing light irradiation that creates electron-hole pairs and then generates reactive oxygen species (ROS), including superoxide anion ($\cdot O_2^-$), singlet oxygen ($^1O_2$), hydrogen peroxide (H_2O_2) and hydroxyl radical (·OH) [19,20]. Overall, the wide-spectrum antibacterial activity and negligible drug resistance have resulted in the considerable development of phototherapy strategies in the antibacterial field [21,22]. Despite the advantages, poor tissue penetration depth and unavoidable phototherapeutic tissue damage have limited their clinical applications. The implementation of PTT individually in the antibacterial process tends to cause damage to the surrounding healthy tissues due to the diffusion of high temperature whereas effective bacterial killing is difficult to be achieved at relatively low temperatures [23]. Similarly, normal tissue lesions may occur in a single-modality PDT antibacterial with the spread of high concentrations of ROS [24]. Therefore, to avoid the limitations of a single treatment method, a synergistic approach of phototherapy with other therapies has been widely implemented, which can achieve better therapeutic effects [25–30]. For example, Deng et al. developed gold nanorods which was coated with polydopamine (PDA) and silver ions (Ag^+) to efficiently eliminate bacteria and promote wound healing through the combined effect of CDT/PTT [26]. Besides, Wu et al. designed a TiO_2-modified Ag_3PO_4 nanoparticle, which could achieve efficient antibacterial activity through the synergistic effect of PDT and ion therapy [27]. Furthermore, they proposed a non-invasive treatment strategy by embedding sodium ions in prussian blue to deal with deep bacterial infections through the synergistic effect of MWT, PTT, and CDT [28].

Due to the advantages of easy availability, high chemical stability, and suitable energy band structure, graphite-phase carbon nitride (g-C_3N_4, CN), a two-dimensional nanosheet, has currently received widespread attention and becomes a research hotspot in the fields of photocatalysis, environmental remediation and biomedicine [31,32]. Notably, CN could split water molecules to produce oxygen under the irradiation of sunlight, which could relieve hypoxia and enhance the PDT effect [33,34]. Nevertheless, the ROS generation of CN is relatively low because of its high recombination rate of photo-generated electron-hole pairs [35]. To address this challenge, the coupling of CN with other semiconductors to form nano-heterojunctions is an effective strategy to enhance photocatalytic efficiency [36–39]. Molybdenum disulfide (MoS_2), with photothermal effect and peroxidase-like activity, has been applied in the antibacterial field [40–42]. The suitable band edge position of MoS_2 and the good lattice matching with CN could enhance the light collection and promote the separation of photo-generated charges [43]. In addition, MoS_2 exhibits strong light-matter interaction, high carrier mobility and spin characteristics, and weak van der Waals force combination. Therefore, the combination of MoS_2 with CN may exert multi-modality synergistic antibacterial functions and avoid the disadvantages of a single-modality treatment.

In the process of cutaneous infection, bacteria have a desperate demand for glucose uptake to fuel their rapid growth [44]. Thus, reducing glucose concentration at the bacterial infection site can profoundly block bacterial growth. Glucose oxidase (GOx), an endogenous oxidoreductase enzyme in organisms, can catalyze glucose into gluconic acid and H_2O_2, which enables the rapid glucose consumption at the infection site [45,46]. Moreover, when GOx is used in combination with photosensitive materials or Fenton-like reagents, the generated H_2O_2 could be further catalyzed into highly germicidal ROS, leading to an excellent cascade and synergistic antibacterial effect [47,48]. Therefore, the combination of GOx with other therapies such as PTT, PDT, or CDT could further elevate the antibacterial effect and enrich the strategy of antibacterial therapy.

Given the aforementioned considerations, we propose a new concept of cascade bio-heterojunctions (C-bio-HJs) consisting of CN/MoS_2 heterojunctions (CN/M bio-HJs) and GOx. The CN/MoS_2 heterojunctions are firstly fabricated *via* the hydrothermal method, followed by GOx loading onto the surface. In the designed C-bio-HJs system, photogenerated electron-hole pairs of CN are remarkably separated with the combination of MoS_2, which could dramatically escalate the photodynamic antibacterial effect of CN. Moreover, as an agent with excellent performance in converting light into heat, MoS_2 can empower CN/M/GOx with robust photothermal antibacterial properties. Furthermore, GOx can effectively consume glucose in diabetic wounds and generate a plethora of H_2O_2, which achieves the starvation therapy effect. Therefore, the cascade antibacterial effect integrating PDT, PTT, and CDT is explored in detail in the present study. As a proof-of-concept, both *in vitro* and *in vivo* experiments were done to verify the antibacterial and biological efficiency of the proposed C-bio-HJs.

2. Materials and methods

2.1. Synthesis of C-bio-HJs

The CN was manufactured by a traditional method through thermal polymerization [49]. In detail, 5 g of melamine (Chengdu KeLong Reagent, China) was placed into a ceramic crucible with a cover (50 mL in volume) and then calcined in a muffle furnace with a ramp rate of 10 °C/min for 4 h at 600 °C. Finally, a yellow solid was attained cooling from the muffle furnace to room temperature.

A one-step hydrothermal method was used to synthesize g-C_3N_4/MoS_2 (CN/M). Briefly, 1 g of CN was sonicated for 2 h to form a homogenous dispersion in 100 mL deionized (D.I.) water. In parallel, a certain amount of ammonium paramolybdate ($H_{32}Mo_7N_6O_{28}$)/thiourea (CH_4N_2S) tetrahydrate (see Table 1 for the specific mass ratio) (Chengdu KeLong Reagent, China) was dissolved in the same volume of D.I. water. The two solutions mentioned above were mixed by vigorous stirring and then sealed in a Teflon-lined stainless steel autoclave with nickel and heated at 180 °C for 12 h. After the reaction, CN/M was washed three times with ethanol and water, filtered, and then dried at 60 °C.

To obtain GOx-decorated samples, 20 mg CN/M was firstly added to the dopamine solution (100 mM) with Tris/HCl buffer (50 mM, pH = 8.5) and stirred overnight. Then, 200 μL of GOx (2 mg/mL in PBS, Aladdin, Shanghai) solution was tethered to the above PDA-modified CN/M material, which was soaked for 12 h. Finally, CN/M/GOx C-bio-HJs were obtained by washing three times with PBS and then drying in an oven at 37 °C.

2.2. Materials characterisation

The sizes and surface morphologies of the materials were observed *via* field-emission scanning electron microscopy (FE-SEM, JSM-7610F,

Table 1
The ingredients list of CN/MoS_2 heterojunction synthesis.

	CN/M0.1	CN/M0.15	CN/M0.2	CN/M0.25
CN	1.0 g	1.0 g	1.0 g	1.0 g
$H_{32}Mo_7N_6O_{28}$	0.1 g	0.15 g	0.2 g	0.25 g
CH_4N_2S	0.2 g	0.3 g	0.4 g	0.5 g

JEOL, Japan). The microscopic morphologies and crystalline structure of samples were further characterized using a transmission electron microscope (TEM) equipped with high-resolution Energy Dispersive Spectrometer (EDS) (TEM, JEM-F200, JEOL, Japan). The phase structure was characterized by powder X-ray diffractometer (XRD, XRD-6100, SHIMADZU, Japan) with Cu Kα radiation with a measuring angle ranging from 10° to 90°. The optical absorption properties of samples were determined by ultraviolet–visible diffuse reflectance spectroscopy (UV–vis DRS), and the data were fitted using the Tauc plot method. The extension line set from the image region of linear approximation perpendicular to the x-axis was the wide-band gap semiconductor. X-ray photoelectron spectroscopy (XPS, AXIS Supra, Kratos, USA) analysis was performed to measure the elemental composition of the CN/M heterojunction. XPS valence band spectra were used to derive the valence band positions of MoS_2 and CN. Raman spectroscopy was performed to confirm whether MoS_2 was successfully loaded onto the surface of CN by probing their vibrational states. The junction of CN and MoS_2 was verified by Fourier Transform Infrared spectrometer (FTIR, Nicolet iS50, Thermo Scientific, USA). The zeta potential before and after loading of GOx was evaluated using Zetasizer Nano ZS (Malvern, England). The separation of the electron-hole pairs in the heterojunction was investigated by comparing the photoluminescence (PL) spectra of CN and CN/M.

2.3. Density functional theory calculations

The Vienna Ab initio Simulation Package was used to perform first-principles calculations in an attempt to elucidate the surface electron transfer mechanism of CN and MoS_2. Furthermore, the projector-augmented wave method was used to evaluate the valence-core electron interaction, and the transfer of electrons and connected interaction was explained using the GGA PBE function. In addition, a conjugate gradient algorithm was used to optimize the structure of CN, MoS_2, and CN/M at the same time. To obtain a more realistic portrayal of the intermolecular interaction at the bio-HJs interface, the van der Waals interaction was evaluated using Grimme's DFT-D3 correlation [50]. In particular, the plane-wave basis function's dynamic energy cut-off was set to 400 eV. A $3 \times 3 \times 1$ k-point grid was used to resolve the Monkhorst-Pack meshes. The convergence criterion for energy was established at 1×10^{-4} eV, and the shape of the ground-state atoms was optimized by lowering the force to 0.05 eV/Å. Furthermore, the change in energy (ΔE) for O_2 adsorption by CN/M was calculated using the equation below:

$$\Delta E = E_a - E_0 \quad (1)$$

where E_a denotes the gross energy of the O_2 adsorbed CN/M and E_0 denotes the energy of the pure CN/M surface.

2.4. Photothermal performance

To evaluate the photothermal performance, a Xenon (Xe) lamp simulated solar light (100 mW/cm^2), NIR laser (808 nm, 1.5 W/cm^2), and dual light (Xe lamp first and then 808 nm laser) was chosen as the light conditions. Firstly, 10 mg samples of CN, MoS2, CN/M0.1, CN/M0.15, CN/M0.2, and CN/M0.25 were disseminated in PBS (10 mL) and continuously exposed to light for 20 min. Then, the photothermal effect was evaluated by recording the temperature change of CN/M0.2 bio-HJs suspension (50, 100, 200, 500, and 1000 μg/mL), each with a 1-min interval, and irradiated by dual light. In addition, all photothermal images were captured by a thermal imager (FLIR-E6, FLIR). Furthermore, the photothermal stability of C-bio-HJs was investigated. The CN/M0.2 bio-HJs solution (200 μg/mL) was irradiated under dual light. The light was then turned off after a continuous 10-min exposure and allowed to drop to ambient temperature naturally, a process that was replicated five times. The photothermal stability was explored using the temperature recorded at 1 min of each interval.

2.5. Oxygen generation

20 mg samples of CN, MoS_2, CN/M0.1, CN/M0.15, and CN/M0.2 were disseminated in 10 mL of deoxygenated PBS before being sealed with liquid paraffin. The solution was irradiated for 20 min with a Xe lamp, and the time-dependent O2 concentration was measured using a real-time oxygen concentration meter.

2.6. Photocatalytic performance

2.6.1. Electron spin resonance (ESR) detection

The ESR spectrometer was further used to verify the ·OH and $\cdot O_2^-$ generation of CN/M0.2. Briefly, 1 mL of sample (1 mg/L) and glucose solution (5 mg/L) were mixed for 30 min and then illuminated by a 808 nm laser for different time points (0, 10, and 30 min). After the illumination, 5,5-dimethyl-1-pyrroline N-oxide (DMPO) was added as a trapping agent for testing.

2.6.2. Generation of hydroxyl radical (·OH)

The ·OH generation was measured using methylene blue (MB, Aladdin) as the detection agent. Briefly, 700 μL (1 mg/L) of sample was first added into MB solution (20 mg/L, 4.3 mL), and then the mixture was incubated statically in darkness for 30 min at room temperature until the adsorption-desorption equilibrium was reached. Subsequently, 1 mL of glucose solution (5 mg/L) or H_2O_2 (10 mM) was added to the solution. The system was left to react for 60 min, and the absorbance spectra were then measured using a UV–vis spectrophotometer (UV1800PC, AoE, China) in the range of 550–750 nm.

2.6.3. Consumption of glutathione (GSH)

Ellman's test was used to assess the capacity of substances to deplete GSH through quantitative analysis of free thiols. Each experimental group (2 mg/L, 50 μL) was mixed with GSH (1 mM, 450 μL) in PBS (pH = 8) and incubated for 60 min in darkness. Simultaneously, a similar concentration of GSH solution (1 mM, 500 μL) with or without H_2O_2 (0.1 mM, 50 μL) was adopted as negative and positive controls, respectively. All samples were exposed to light for 10 min after incubation. Then, tris/HCl buffer (50 mM, pH = 8.0, 450 μL) and 5,5'-dithiobis-(2-nitrobenzoic acid) (DTNB, Aladdin, 1 mM, 100 μL) were incorporated into the solution. After 30 min of reaction, the absorption of the supernatant at 410 nm was measured using a UV–vis spectrophotometer throughout 250–550 nm.

2.6.4. Detection of singlet oxygen

The generation of single oxygen was determined using 1,3-diphenylisobenzofuran (DPBF, Aladdin) as the probe. The CN, MoS_2, CN/M0.2 in D.I. water (1.5 mg/mL) was mixed uniformly with DPBF (2 mg/mL in DMSO) for 10 min in darkness. Each sample was continuously illuminated for 0, 25, 50, 75, or 100 s, and the absorption of the supernatant was detected using a UV–vis spectrophotometer ranging between 300 and 500 nm.

2.7. In vitro antibacterial performance evaluation

2.7.1. Bacterial culture

Escherichia coli (E. coli, ATCC 25923*)* and *Staphylococcus aureus (S. aureus,* ATCC 25923*)* were utilized to assess the antibacterial efficacy. The strains were grown using liquid broth (LB) medium that contained beef extract (0.3 g), polypeptone (1 g), glucose (0.5 g), and D.I. water (100 mL), while the solid medium was supplemented with additional agar powder (2.3 g, Aladdin). The entire LB medium was sterilized through autoclaving before the experiment.

2.7.2. The antibacterial activity assay

The number of surviving bacteria was determined by spread plate assay to calculate the antibacterial ratio after darkness, Xe lamp, 808 nm laser, and dual light irradiation treatments, which was associated with the antibacterial properties. The bacteria were cultured in LB media as described previously and were incubated at 37 °C with constant shaking until the medium was turbid. Finally, the bacteria were collected and enumerated, and diluted to a concentration of 1×10^5 CFU/mL. Then, 40 μL of the nanomaterial suspension (200 μg/mL) was mixed with 160 μL of bacterial liquid and illuminated for 10 min. The bacterial suspension was therefore covered on agar plates and cultured for 24 h at 37 °C. Following that, the bacterial colonies were photographed and quantified by computing the antibacterial ratio using the equation below (2).

$$\text{Antibacterial ratio } (\%) = (C\text{-}C_n)/C \times 100\% \quad (2)$$

where C and C_n represent the number of bacteria in the control and experimental groups, respectively.

2.7.3. Bacterial characterisation by SEM

Briefly, 1×10^7 CFU/mL of bacterial suspension was treated with different samples, and bacterial suspension with no sample was served as the control group. After 10 min of light/dark treatment, the samples were fixed in 2.5% glutaraldehyde for 2-4 h before being dehydrated for 15 min with a gradient ethanol solution with concentrations ranging from 30% to 100% (*v/v)*. SEM was then used to examine the bacterial morphology.

2.7.4. Bacterial viability analysis by live/dead staining

To visualize the live and dead state of microorganisms, Live/Dead staining (Aladdin) was applied. Briefly, 1×10^7 CFU/mL of bacteria were cultured in a 48-well plate for 12 h, and then samples at different concentrations were added into bacterial suspension under light exposure for 10 min. The bacteria were rinsed three times with water and stained for 15 min with SYTO9 (green colour denotes living bacteria) and PI (red colour denotes dead bacteria). The bacteria were examined by fluorescence microscopy after three times of washing.

2.8. Cell culture

Cell culture experiments were performed using mouse L929 fibroblasts that were purchased from ATCC (USA). All cells were grown in DMEM (high-glucose, Gibco, USA) supplemented with 10% FBS (Gibco, USA) and 1% penicillin-streptomycin (Beyotime, Shanghai) at 37 °C in 5% CO_2, and the culture medium was renewed every 2 days.

2.8.1. Cell proliferation and morphology

The CCK-8 test was used to assess the proliferation and viability of L929 cells (Beyotime, Shanghai). In 48-well plates, L929 cells were seeded at a density of 1×10^4 cells/well and subsequently incubated with the prepared nanomaterial suspension (200 μg/mL). Each well was filled with cell culture media containing 10% CCK-8 reagent and co-cultured for 1, 3, or 5 days. After incubating the cells in the dark for 1 h, 1100 L of cell medium was moved to a 96-well plate for measurement. The optical density (OD) of the supernatant at $\lambda = 450$ nm was measured using a microplate reader (SAF-6801, BAJIU, China).

2.8.2. Cytotoxicity assay

Cell cytotoxicity test was conducted using a calcein/propidium iodide (calcein/PI) staining kit (Beyotime, Shanghai). To begin, L929 cells were planted at a density of 1×10^4 cells/well in 48-well plates for 1-3 days, with medium replaced every other day, until the cells achieved roughly 90% confluency. The Live/Dead working solution (2 M AM, 8 M PI) was then added to the well plates seeded with cells as described above, after 2 h incubation, the stained cells were observed under a fluorescence microscope (CKX53, OLYMPUS, Japan).

2.9. Animal experiments

2.9.1. Establishment of infectious skin wound model

All animal experiments in this work were authorized and followed the instructions of the Animal Care and Experiment Committee of the West China Hospital of Sichuan University (No.2021605A). Furthermore, all animals were housed and handled in full conformity with the National Regulation of China for the Care and Use of Laboratory Animals. The Balb/c mice aged 4-6weeks (17-25 g) are acclimatized to husbandry conditions for at least 3 days before the experiment. Firstly, according to the standard protocol, modeling could be started after 1 week of acclimatization on normal chow, fasting for more than 12 h. A single dose of approximately 200 mg/kg of streptozotocin (STZ, Sigma) solution was injected into all-male mice to establish a diabetes model. To show that the mice were diabetic, blood glucose levels in tail vein blood were monitored 7 days after injection using an electronic glucometer, and body weight was recorded. (Accu-Check Performa, Roche Diagnostics, USA). Hyperglycemia mice (e.g. blood glucose levels of more than 16.7 mmol/L and weight loss) were chosen for further research.

To construct the infectious wound model, mice were firstly anesthetized with 2% sodium pentobarbital (10 mL/kg) in general, and an 8 mm diameter circular incision was made on the dorsal side of the shaven hair mice. Then, 20 μL of *S. aureus* was injected onto the incision, which was covered with clear airtight tape. (1×10^7 CFU/mL). After being kept in an anaerobic environment for 24 h, an obvious inflammatory wound was obtained. Next, the mice were selected and divided randomly into four experimental groups as follows: dark, Xe lamp, 808 nm laser, and dual light. Then, 10 μL of the C-bio-HJs suspension (200 μg/mL) was applied to the wound and then treated in the dark or under illumination. Regarding the illumination group, Xe lamp (100 mW/cm^2), 808 nm laser (1.5 W/cm^2), and dual light (Xe lamp first and then 808 nm laser) was used. Similarly, PBS was used as blank control without treatment. To minimize burns, wounds were kept moist during the treatment by using normal saline (0.9%). The thermogram of each mouse was recorded at 5-min intervals using a thermal infrared imager. Then, after each group of wounds was treated with light or in the dark for 10 min, wound exudate from each mouse was extracted with 1 mL of sterile saline and deposited in a centrifuge tube containing 1 mL of sterile PBS, which was used to assess the wound infection. The body weight and wound area of mice were recorded and photographed at 1-, 3-, 5- and 7-day intervals, and mice were sacrificed on day 7. The tissues around the wounds were collected and fixed for histological analysis. In addition, blood was collected from the veins in the tail for routine blood biochemistry analysis.

2.9.2. Assessment of wound healing

To monitor the process of wound healing, the wound area was photographed and documented every day with a digital camera. The relative wound area was calculated using the equation below.

$$\text{Relative wound area} = A_n/A_i \times 100\% \quad (3)$$

A_i represents the original wound area, A_n represents the wound area treated with various samples on days 1, 2, 3, 4, 5, 6, and 7.

2.9.3. In vivo antibacterial efficiency

The number of surviving bacteria was determined by plate assay to calculate the antibacterial ratio. First, we collected bacteria *in vivo*, specifically, after the mice were exposed to light for 10 min, the secretion from the wound was collected with a cotton swab into an EP tube containing PBS, and then the supernatant was transferred to an LB medium for incubation, and surviving bacteria were obtained after 24 h. The bacterial colonies were counted and photographed. Finally, the antibacterial efficiency was calculated by the previous equation (2).

2.9.4. Histopathologic analysis

Tissue samples surrounding the wound were collected and fixed for 24 h in 4% paraformaldehyde. H&E staining was utilized to get a proper view of the infected wounds. Furthermore, Masson's trichrome staining was used to calculate the changes in healing processing *via* collagen fibers. Light microscopy (DMI 4000, Leica. Germany) was used to capture the images. Immunohistochemical staining for TNF-α, CD34, and Giemsa as well as immunofluorescence staining for VEGF, were used to examine the expression of inflammation-related proteins and tissue regeneration. To assess the *in vivo* biocompatibility of the C-bio-HJs, the hearts, livers, spleens, lungs, and kidneys of euthanized mice were stained with H&E.

2.10. Statistical analysis

The above tests were done three times and the results were represented as mean standard deviation ($n \geq 3$). All quantitative data were subjected to one-way ANOVA or two-way ANOVA, with significant differences calculated. Within the research, values of $^{*}p < 0.05$ and $^{**}p < 0.01$ were considered statistically significant.

3. Results and discussion

We create a CN/M/GOx C-bio-HJs therapeutic system that produces a glucose oxidase-primed dynamic therapy with rapid antibacterial properties and tissue repair capabilities. As depicted in Scheme 1, briefly, g-C_3N_4 nanosheets are first synthesized from melamine, and

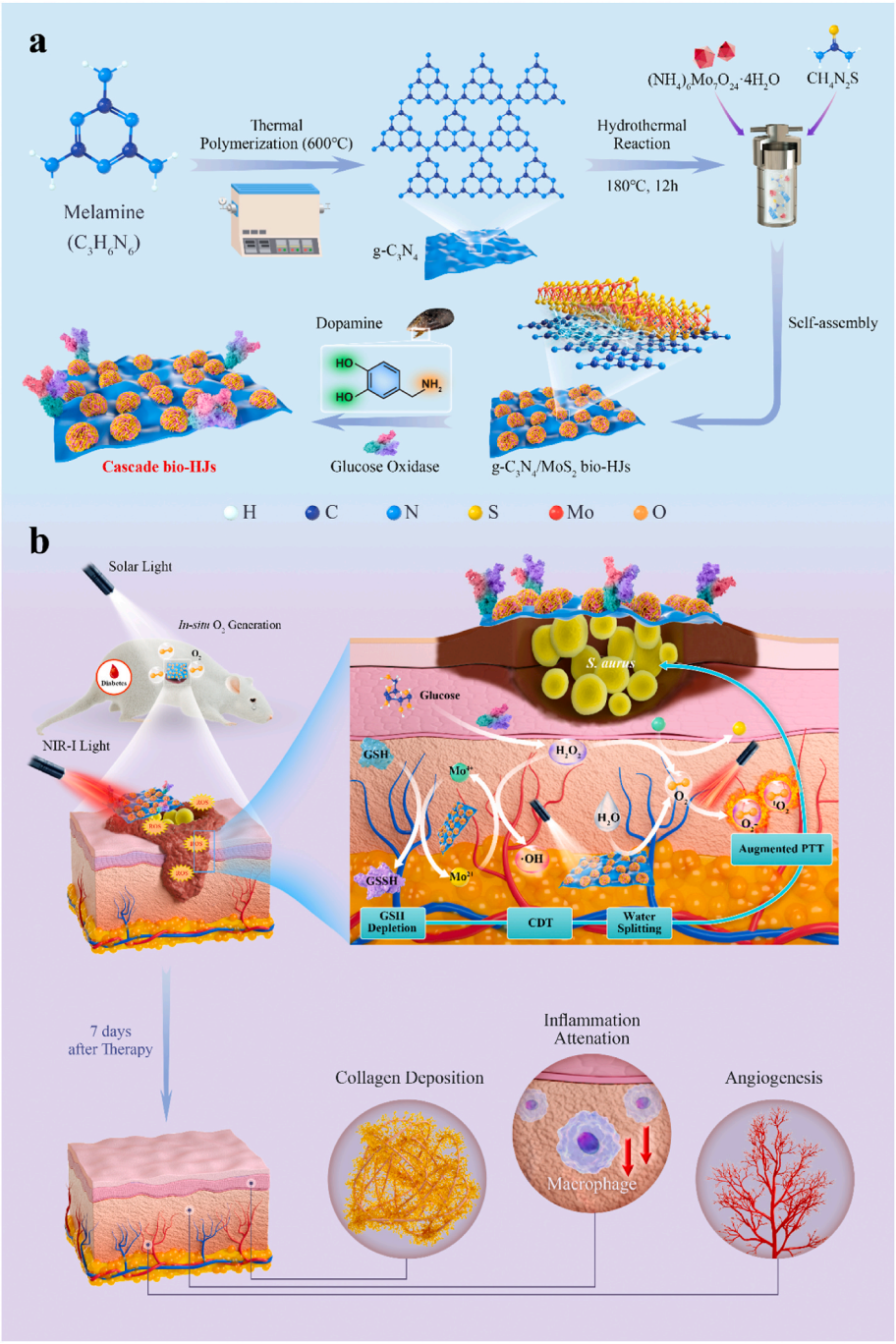

Scheme 1. (a) Synthesis of the g-C_3N_4/MoS_2-based C-bio-HJs; (b) The GOx-primed cascaded antibacterial actions for the remedy of infected cutaneous regeneration.

then transition metal MoS_2 is introduced *via* hydrothermal reaction to prepare CN/MoS_2 bio-HJs. Next, the CN/M/GOx C-bio-HJs therapeutic system is created by using dopamine-loaded GOx, and its bactericidal properties have been investigated. Furthermore, dual light irradiation is used in this study. On the one hand, the presence of MoS_2 can promote the photo-generated electron-hole separation to enhance the photocatalytic ability of CN and endow it with excellent photothermal properties, allowing C-bio-HJs to exert PTT and PDT under 808 nm laser; on the other hand, solar light can cause g-C_3N_4 to split water to generate more O_2, allowing C-bio-HJs to generate a large amount of ROS, which greatly solves the problem of insufficient oxygen supply to deep tissues during PDT. At the same time, because MoS_2 possesses properties of the Fenton-like reaction, it serves as a catalase-like catalyst. When GOx catalyzes the production of H_2O_2 from glucose, the H_2O_2 can subsequently be decomposed by MoS_2 into extremely toxic ·OH, resulting in high-performance CDT. After 7 days of treatment with C-bio-HJs, the

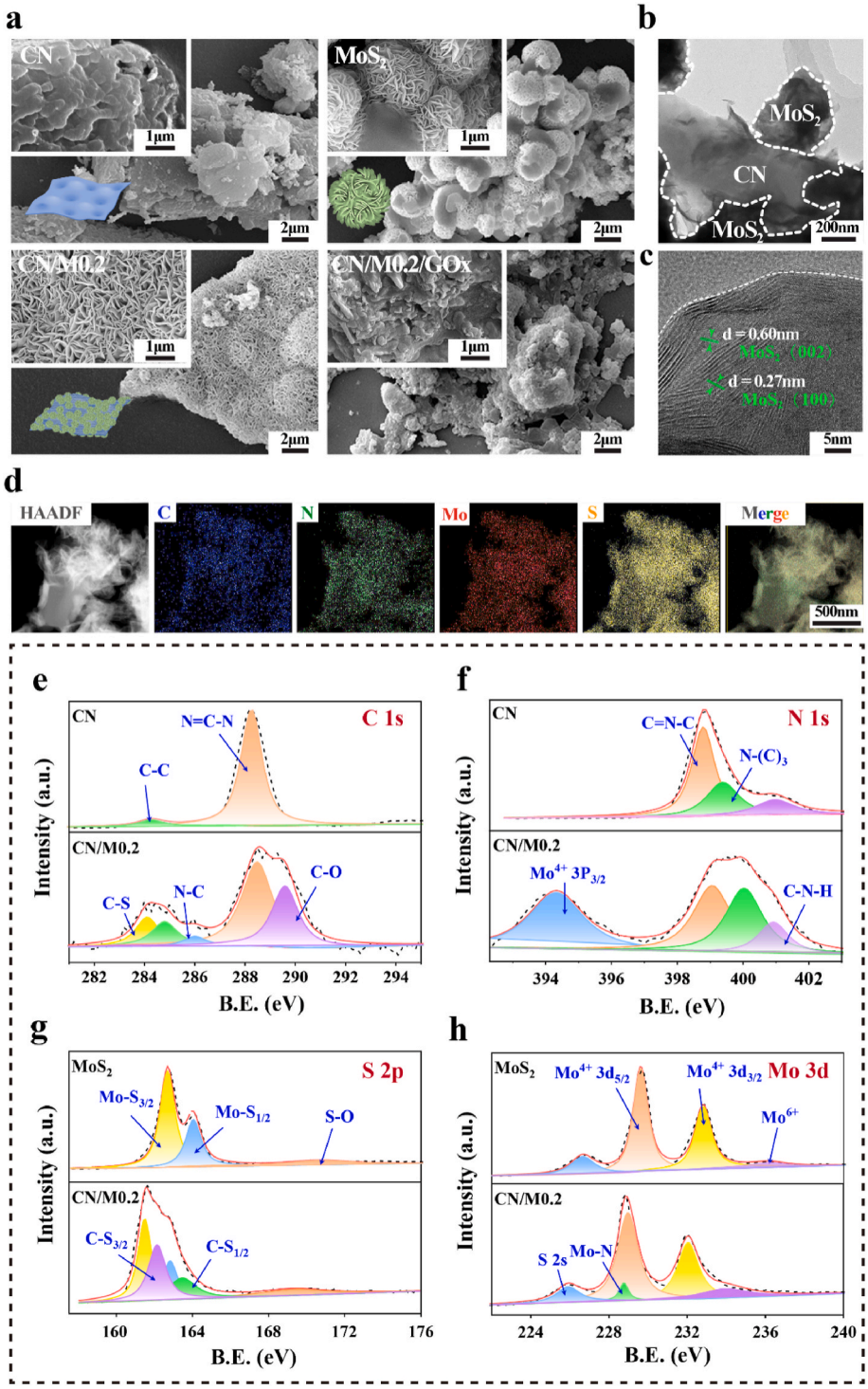

Fig. 1. The FE-SEM images of (a) CN, MoS_2, CN/M0.2, and CN/M0.2/GOx samples; (b) TEM, and (c) HR-TEM images of the CN/M0.2 bio-HJs, (d) EDS mapping of C, N, S and Mo of CN/M0.2; (e, f) The high-resolution XPS spectra of C 1s and N 1s for CN and CN/M0.2; (g, h) The high-resolution XPS spectra of S 2p and Mo 3d for MoS_2 and CN/M0.2.

inflammation in animal wounds is reduced, collagen begins to deposit, new blood vessels are formed, and wound repair is significantly improved. Ultimately, the C-bio-HJs achieves a multimodal antibacterial effect by integrating with PDT, PTT, and CDT.

3.1. Preparation and characterisation of C-bio-HJs

The morphology and structure of each product during the synthesis process were firstly characterized by FE-SEM. As shown in Fig. 1a, CN exhibits a laminated block structure formed by lamellar nanosheets, whereas MoS_2 has a typical flower-like structure stacked by several uniform-sized nanoleaves with a diameter of approximately 2 μm observed under higher magnification [51]. For the CN/M bio-HJs sample, MoS_2 nanoclusters are evenly covered on the surface of CN, indicating that the CN/M bio-HJs is successfully fabricated. After combination with GOx, the nano flower-like structure is not as clear as observed earlier, and the surface of CN/M is coated with a thin film-like substance, indicating the successful loading of GOx. Then, the structure of CN/M0.2 bio-HJs was further characterized and analyzed by TEM. As shown in Fig. 1b, CN/M0.2 bio-HJs exhibits a typical two-dimensional structure because of the close combination of CN and MoS_2. In addition to this, two series of clear mesh fringes with lattice spacings of 0.27 and 0.6 nm are present, corresponding to the plane (100) and (002) of the MoS_2 hexagonal plane (green arrows in Fig. 1c). Simultaneously, the EDS mapping images of the selected area of CN/M0.2 also show the presence of C, N, Mo, and S (Fig. 1d), which proves that MoS_2 and CN are tightly integrated and validates the successful fabrication of CN/M0.2 bio-HJs.

We used XPS to analyze the surface elemental composition of the sample, as well as the interaction between MoS_2 and CN. Fig. 1e-h shows the signal peaks deconstructed from the high-resolution spectra analysis of each element in CN, MoS_2, and CN/M0.2. The C 1s spectra of CN and CN/M0.2 (Fig. 1e), deconstructed five peaks matching the C–C bond, N═C–N bond, C–S bond-C-N bond-C-O bond, respectively. When compared to the C 1s pattern of pure CN, the existence of C–S bonds (284.08 eV) in CN/M0.2 indicates that MoS_2 is successfully doped. And the N═C–N peak of CN/M0.2 shifts to the high binding energy position by approximately 0.25 eV, perhaps due to the decline of electron density around C atoms in CN/M0.2. The above-described results indicate that a strong interaction exists between MoS_2 and CN. For the N 1s spectrum, as shown in Fig. 1f, both CN and CN/M0.2 can decompose three consecutive peaks that match the sp^2 hybridized N (C═N–C) on the triazine ring, tertiary nitrogen bond (N-$(C)_3$) combined with carbon and the amino functional group (C–N–H), respectively. Here the functional groups between CN and CN/M0.2 remain unchanged, indicating that the structure of CN is stable during the hydrothermal reaction. However, it should be noted that all the peaks of C═N–C, N-$(C)_3$, and C–N–H have shifted in CN/M0.2, and the N-$(C)_3$ area increases significantly. Fig. 1g shows the S 2p XPS spectra of MoS_2 and CN/M0.2, the peaks of S 2p3/2 and S 2p1/2 of pure MoS_2 are 162.47eV and 163.66 eV, respectively. In contrast, the respective peaks of CN/M0.2 are 161.51 eV and 162.80 eV, which are reduced by 0.96 eV and 0.86 eV, respectively, indicating there is a directional electron transfer between CN and MoS_2. At the same time, according to the Mo 3d XPS spectra of MoS_2 and CN/M0.2 (Fig. 1h), similar to the above results for S 2p, the 3d peak of Mo also shifts towards lower binding energy, further verifying the above-mentioned electron transfer result. Furthermore, the CN/M0.2 sample in Fig. 1g exhibits two additional peaks of C–S 2p3/2, C–S 2p1/2 at 162.13 eV and 163.43 eV, and a Mo–N peak at 228.73 eV also appears in Fig. 1h, confirming that C–S and Mo–N bonding are formed through the chemical bonding. These results also convince us that the CN/M0.2 bio-HJs is successfully formed.

After confirming the surface chemistry of the materials, XRD was further used to analyze the phase structure and crystallinity of the synthesized samples. Fig. 2a shows the two typical diffraction peaks of CN at 14.8° and 27.4°, which are attributed to the repeated in-plane and interlayer conjugated heptazine unit of the aromatic carbonitride system, indicating the successful preparation of CN (JCPDS no. 87–1526). It is also found that there is almost no change in the XRD peak of CN after the doping of MoS_2. The CN/M bio-HJs samples contain two peaks at 33.5° and 57.7°, which may be attributed to the faces (100) and (110) of the hexagonal MoS_2 (JCPDS no. 37–1492). Interestingly, all samples have no diffraction peak at the (002) crystal of MoS_2, suggesting that MoS_2 prepared by the hydrothermal method is a nanosheet with a few layers, which is advantageous to the heterojunction's photocatalytic performance. Raman spectroscopy was further used to characterize the

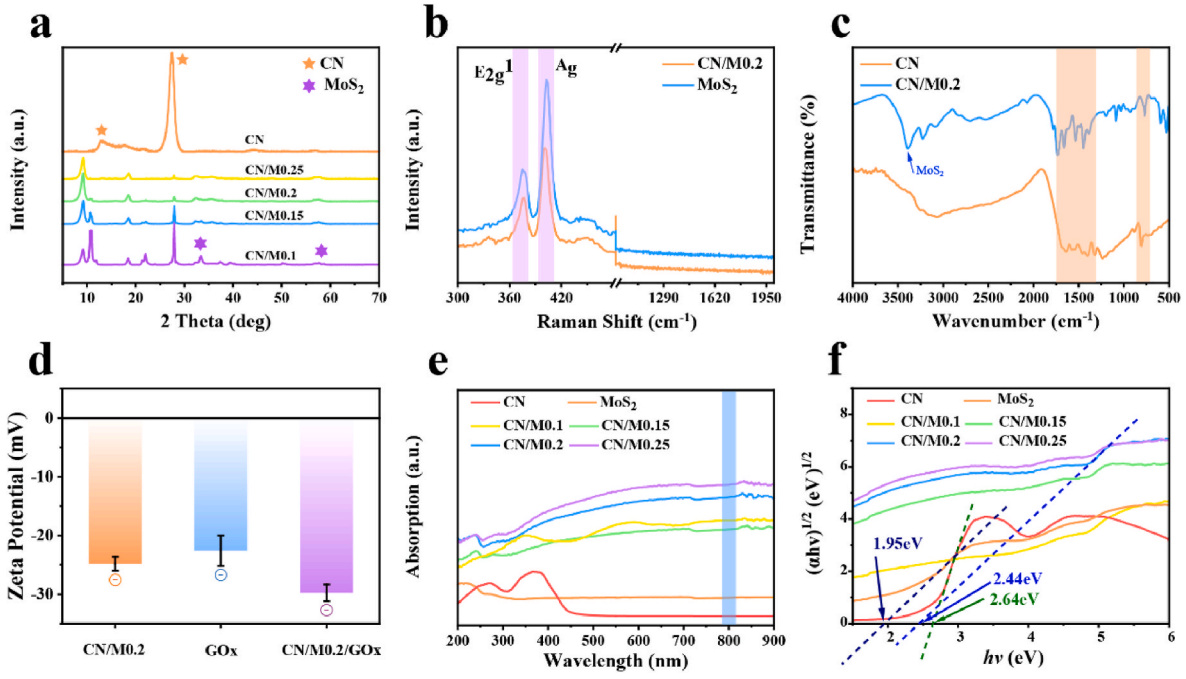

Fig. 2. (a) XRD patterns of different samples; (b) Raman spectra of MoS_2 and CN/M0.2; (c) FTIR spectra of CN and CN/M0.2; (d) Zeta potential of different samples. (e) UV–Vis absorption spectra of each sample; (f) The band gap of each sample calculated by the Tauc plot method.

composition and structure of the heterojunction. As shown in Fig. 2b, there are two strong peaks located near 375. 8 cm^{-1} and 470. 8 cm^{-1} in the Raman spectra of CN/M0.2 and MoS_2, which correspond to the E^1_{2g} and A_{1g} photon vibration modes of MoS_2, respectively. These results jointly demonstrate that we have synthesized a type of high-quality CN/M bio-HJs through the hydrothermal method and are also corroborated with TEM and XRD analysis results. In addition, it can be found that the peak intensity of CN/M0.2 is significantly lower than that of pure MoS_2 due to the strong interaction between CN and MoS_2 [52]. Moreover, the MoS_2 Raman vibration mode E^1_{2g} is blue-shifted, and that of A_{1g} is red-shifted, indicating that the layer number of MoS_2 is reduced after combined with CN [53], which is highly beneficial for the photocatalytic performance of CN/M0.2 bio-HJs.

To examine the changes in CN before and after the addition of MoS_2, we affirmed their structures by FT-IR. CN and CN/M0.2 exhibit almost similar characteristic vibration modes as CN. As depicted in Fig. 2c, the characteristic peaks of CN are clearly visible at 800 cm^{-1} and 1200–1620 cm^{-1}, and these peaks are related to the out-of-plane bending of one-sixth of the arson ring and the stretching vibration of γ (C–NH–C) and γ (C═N). Therefore, it can be concluded that the aromatic CN system has a stable skeleton structure. We next measured the zeta potential of each sample to understand the bonding modality of GOx and CN/M0.2. As shown in Fig. 2d, the zeta potential of CN/M0.2 is −24.83 ± 1.18 mV, while GOx is −22.60 ± 2.61 mV, When GOx is combined, the zeta potential of CN/M0.2 decreases from −24.83 ± 1.18 mv to −29.77 ± 1.40 mV, indicating that GOx is attached to the surface of CN/M0.2 bio-HJs through PDA coating [54].

To better elucidate the photocatalytic enhancement mechanism of the prepared material, ultraviolet–visible diffuse reflectance spectroscopy was used to determine the light absorption capability. As depicted in Fig. 2e, pure CN has an absorption edge close to 460 nm, which is consistent with its inherent absorption. This characteristic enables CN to absorb only visible light but not the NIR band. And MoS_2 exhibits strong absorption in the entire wavelength range between 200 and 900 nm (Fig. 2e). After the introduction of MoS_2, the CN/M absorption edge undergoes a significant red shift, which not only expands the absorption spectrum with absorption in the NIR (position marked by the blue background color), but also further enhances the light absorption intensity. It is particularly clear that CN/M0.2 and CN/M0.25 have better light absorption than either neat CN or MoS_2. The results indicate that the light absorption capacity of CN/M bio-HJs is enhanced. Finally, the band gap graph is fitted using the Tauc plot function (Fig. 2f), and the band gaps of pure CN and MoS_2 are 2.64 eV and 1.95 eV, respectively, and compared to 2.44 eV for CN/M0.2. The calculated equation is as follows:

$$(\alpha h\nu)^{1/n} = A(h\nu - E_g) \quad (4)$$

Where α is absorption coefficient, A is a constant, ν is frequency, h is Planck's constant, E_g is a wide-band gap semiconductor, n = 1/2 with a direct band gap, n = 2 with an indirect band gap). $h\nu$ in the x-axis is

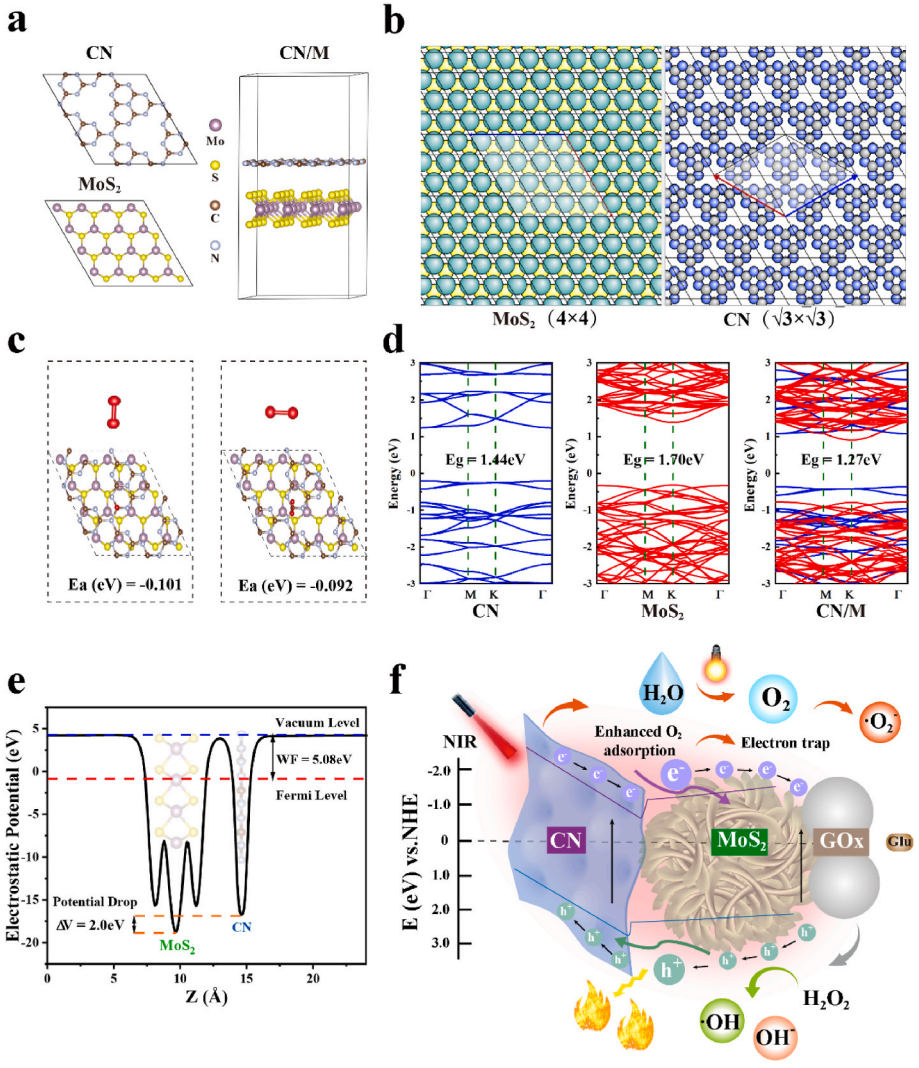

Fig. 3. (a) Crystal structure of CN, MoS_2, and CN/M of different perspectives after structure optimization; (b) The lattice matching method of $MoS_2(4 \times 4)$ and $CN(\sqrt{3} \times \sqrt{3})$; (c) Adsorption structure of O_2 vertical and horizontal absorption onto CN/M, respectively. Red atoms indicate O atoms; (d) Electronic band gap structure of CN, MoS_2, and CN/M; (e) Electrostatic potential of CN/M; (f) The schematic diagram of the electron transfer process between CN and MoS_2 based on DFT calculation and the synergistic treatment mechanism of CN/M/GOx C-bio-HJs.

plotted *vs.* $\alpha h\nu$ in the y-axis.

3.2. DFT calculation

DFT calculation was conducted to demonstrate the interfacial interaction between CN and MoS_2. As shown in Fig. 3a, the structure of the heterojunction is obtained from doped MoS_2 and CN, with the lattice constant being calculated to a = b = 12.710 Å, and the constant corresponding to monolayer MoS_2 and CN is a = b = 3.177 Å and a = b = 7.115 Å, respectively. According to the lattice matching model (Fig. 3b), when a 4 × 4 MoS_2 cell contacts with a $\sqrt{3} \times \sqrt{3}$ CN cell, the tensile stress of lattice mismatch applied to CN is 3.13%, which contains 90 atoms for the entire heterojunction. To better understand the photocatalytic properties, the O_2 adsorption state on the bio-HJs surface was stimulated because O_2 is involved in photogenerated electrons reaction and then affects the generation of ROS [55]. Fig. 3c shows the adsorbed O_2 site on the surface of CN/M bio-HJs in horizontal and vertical adsorption, and the distance between the O_2 molecule and CN is about 3.5 Å, which is approximately similar to the interlayer distance between CN and MoS_2. Moreover, for further exploration, we calculated the adsorption energy for O_2 on the same adsorption sites to facilitate comparison. Specifically, formula (5) is as follows:

$$E_a = E_{O2/heterojunction} - E_{heterojunction} \quad (5)$$

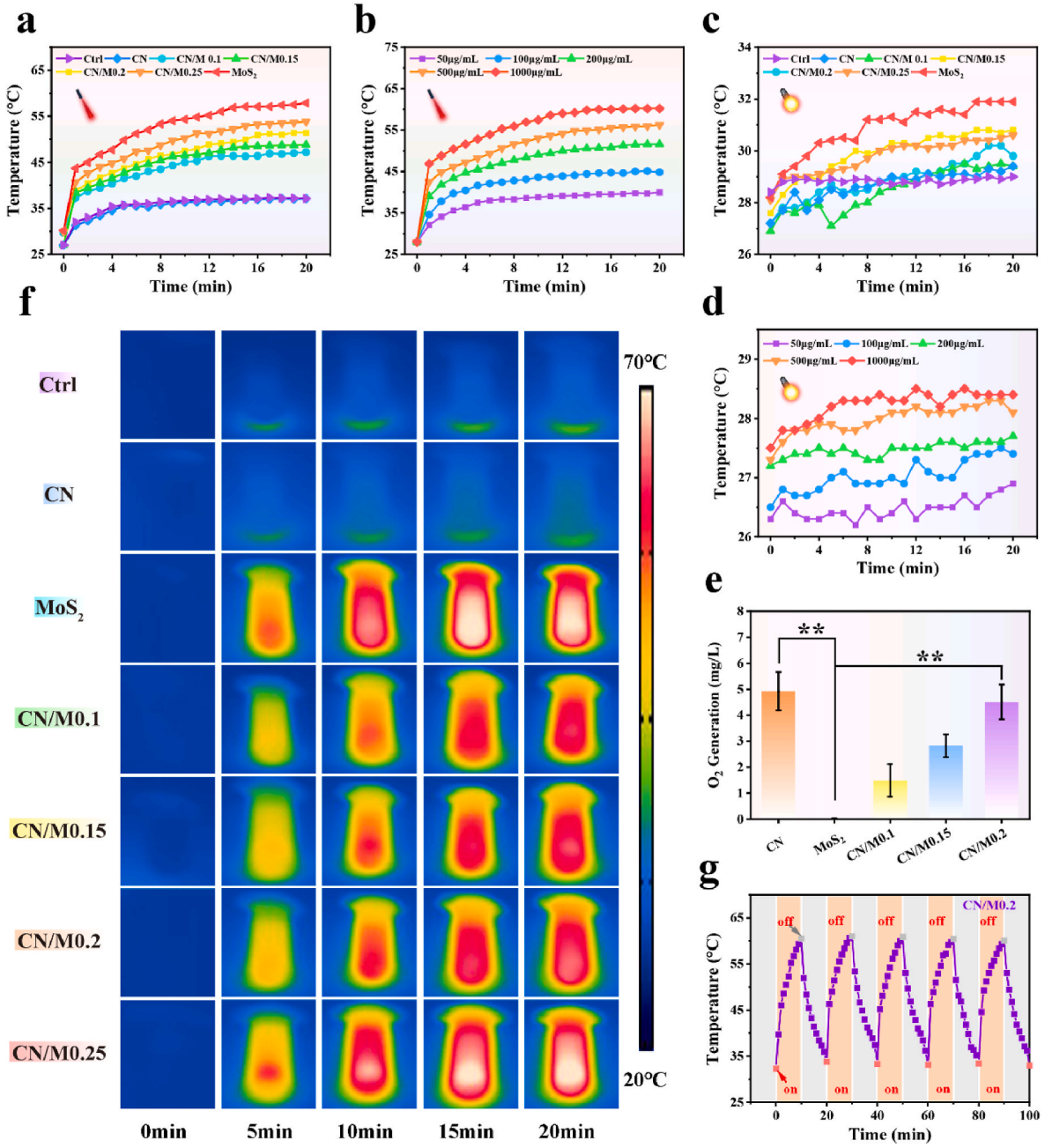

Fig. 4. (a) The heating curves of different samples were continuously exposed under an 808 nm laser for 20 min; (b) The heating curves of CN/M0.2 with various concentrations were continuously exposed to an 808 nm laser for 20 min; (c) The heating curves of different samples exposed to Xe lamp for 20 min; (d) The heating curves of CN/M0.2 with different concentrations exposed to Xe lamp for 20 min continuously; (e) The O_2 generation of different samples exposed to Xe lamp for 20 min; (f) Real-time infrared thermal images of different samples exposed to continuous irradiation; (g) The photothermal cycling curves of CN/M0.2 exposed to the dual light. (* represents $p < 0.05$, ** represents $p < 0.01$).

E_a is the adsorption energy, which is equal to the energy of the heterojunction with O_2 minus the energy of the mono-heterojunction and O_2 molecule. After calculation, it is found that the adsorption energy values are −0.101 eV and −0.092 eV, respectively. This clearly indicates an electron transfer on the interface, as illustrated in Fig. 3f. In this case, O_2 can be adsorbed more due to a redistribution of electrons, which increases the generation of ROS. Fig. 3d illustrates the contribution of the energy band structure of CN (marked in blue curves) and MoS_2 (marked in purple curves), which clearly shows that the band gap of CN/M decreases to 1.27 eV, since the VB and CB of the heterojunction are separately provided by those two structures, and it belongs to a type II heterojunction structure [40]. Here, we would like to point out that the band gap value is calculated from the PBE function in this calculation, which results in an underestimated band gap compared with the experimental band gap (1.95 eV shown in Fig. 2f) [56,57].

However, these results can be used to estimate tendencies, such as an increase or decrease in band gap. To ensure the validation of the band gap reduction results, a heterostructure formed by MoS_2 and CN was again constructed. As shown in Figs. S1a–b, Supporting Information, this sample is more computationally intensive, which contains 113 atoms for the entire heterojunction, and the compression stress of lattice mismatch applied to CN is 2.67%. Besides, Fig. S1c, Supporting Information, shows the corresponding energy gap diagram, confirming that the band gap value has reduced, which is consistent with the above-described analysis result.

3.3. Photothermal and photostability of C-bio-HJs

Heating curves and photothermal pictures were used to assess the PTT potential after 20 min irradiation at 808 nm laser. As shown in Fig. 4a, the final temperature is in the order of MoS_2 > CN/M0.25 > CN/M0.2 > CN/M0.15 > CN/M0.1 > CN, indicating that MoS_2 is the major source of the photothermal effect. Moreover, the temperature of each sample increases rapidly after 10 min of irradiation and then stabilizes, reaching the maximum after 20 min of continuous light exposure. These findings clearly indicate that the CN/M0.2 bio-HJs possesses excellent photothermal conversion efficiency. Based on this result, the CN/M0.2 bio-HJs is selected to evaluate the subsequent photothermal performance for its appropriate final temperature (47.5 °C, Fig. 4a). Fig. 4f shows the photothermal images for each sample, and almost no temperature change is observed in the CN and PBS groups, while the temperature of the other groups is significantly elevated in comparison. This shows that the final temperature of the heterojunction originates from MoS_2, which is consistent with the results of the heating curve in Fig. 4a. However, as shown in Fig. 4b, the final temperature of all samples depends on the level of concentration, wherein the higher the concentration of the sample, the higher the final temperature. This suggests that the temperature of CN/M0.2 bio-HJs can be regulated by the concentration, which will be a high potential application in the antibacterial field.

The heating curve was evaluated utilizing a Xe lamp as the solar light source to further investigate the influence of visible light alone on the photothermal performance of CN, CN/M0.1, CN/M0.15, CN/M0.2, CN/M0.25. As illustrated in Fig. 4c, after the continuous illumination using Xe lamp for 20 min, all samples do not exhibit obvious photothermal performance with a change in temperature of ≤5 °C at any concentration (Fig. 4d). Moreover, under the dual light and 808 nm laser illumination (Fig. S2a, Supporting Information), the photothermal curve of CN/M0.2 is similar to that of 808 nm laser, implying that the Xe lamp cannot trigger the photothermal effect of CN/M0.2. Surprisingly, however, as shown in Fig. 4e, CN has excellent O_2 generation ability, which is retained after the heterojunction is formed with MoS_2. These O_2 will provide a favorable supply for the generation of ROS during the process of PDT. As depicted in Fig. 4g, the temperature of CN/M0.2 exhibits a good photostability with or without the dual light irradiation, and the same phenomenon can also be observed in successive cycles, indicating that the repetitive irradiation does not affect the photothermal properties of the CN/M0.2 bio-HJs.

3.4. Photocatalytic performance

Given that the separation efficiency of the photo-generated electron-hole pairs can greatly influence the photocatalytic activity of a photocatalyst, we employed PL spectroscopy to evaluate the separation efficiency of the electron-hole pair on our CN/M0.2 bio-HJs. As shown in Fig. 5a, the recombination of photo-generated electron-hole pairs produce a strong emission peak at about 460 nm, which is responsible for the strong emission peak of CN. This result implies that pure CN has a strong light absorption capacity, but its electron-hole pairs can easily recombine, making photocatalytic performance poor. In comparison, CN/M0.1 has a stronger PL quenching effect, as CN/M bio-HJs can promote the interfacial electron transfer. Moreover, as the relative content of MoS_2 increases, the PL quenching effect becomes more obvious. However, when the MoS_2 content increases to a certain extent, the PL peak intensity increases instead (CN/M0.25 > CN/M0.2), because a high MoS_2 content may provide a platform for the recombination of the electron-hole pairs.

To assess the ROS yield efficiency in greater depth, we detected the generation of $^1O_2$ using the DPBF probe. As expected, the DPBF absorption peak in the CN/M0.2 group decreases with the irradiation time of dual light (Figs. S3a–c), as well as under Xe lamp (Figs. S3g–i), implying the generation of $^1O_2$. We also found that CN/M0.2 consumes much more DPBF than neat CN and MoS_2. The reason for this is that bio-HJs can not only effectively separate photoexcited electron-hole pairs and enhance charge transfer rates, but they can also undertake water splitting of CN, generating oxygen for the formation of more $^1O_2$ [58]. However, the absorption peak of all groups under the 808 nm laser condition displays a negligible change (Figs. S3d–f), indicating that these samples cannot produce $^1O_2$ under 808 nm laser irradiation. Another probe, DMPO, was used to confirm the type of ROS production of CN/M0.2 by ESR under dual light. As shown in Fig. 5b–c, no ESR signal peak appears under dark condition, indicating that CN/M0.2 cannot produce ROS and there is no photocatalytic effect. However, the ESR signal can be clearly detected with 10 min light exposure. As the illumination time is extended to 30 min, the intensity of the signal peak increases. In Fig. 5b, it can be seen that four characteristic peaks are detected under successive excitations and the heights of these peaks are in the ratio of 1:2:2:1, which is convincing evidence for the production of DMPO-·OH. At the same time, a strong ESR signal is observed in Fig. 5c, where the characteristic peak of DMPO-$\cdot O_2^-$ is detected under dual light. This result completely demonstrates that the heterojunction, CN/M0.2 can well promote the separation of photo-generated electron-hole pairs, and more ROS can be generated, confirming the previous PL results.

In recent years, a newly defined CDT effect through increased free radical production by Fenton-like reaction has attracted considerable attention in anti-tumour and antibacterial therapies [47,58]. Our previous study has demonstrated that MoS_2 heterojunction nanomaterials can exhibit outstanding CDT effects on the basis of the Fenton-like reaction [30]. Therefore, to confirm whether CN/M bio-HJs have the potential Fenton-like reaction activity in the present study, we determined the consumption of MB by measuring it in the presence of H_2O_2 and glucose, and the specific mechanism is illustrated in Fig. 5d. As shown in Fig. 5e, in the presence of H_2O_2, MoS_2, CN/M0.2, and CN/M0.2/GOx groups, all show a significant decrease in peak intensity at 660 nm, indicating that ·OH is produced with increasing irradiation time. This is primarily because MoS_2 has peroxidase-like properties and the released Mo^{4+} that can catalyze H_2O_2 to form ·OH [42] (Formula (6)).

$$Mo^{4+} + H_2O_2 \rightarrow Mo^{6+} + \cdot OH + OH^- \quad (6)$$

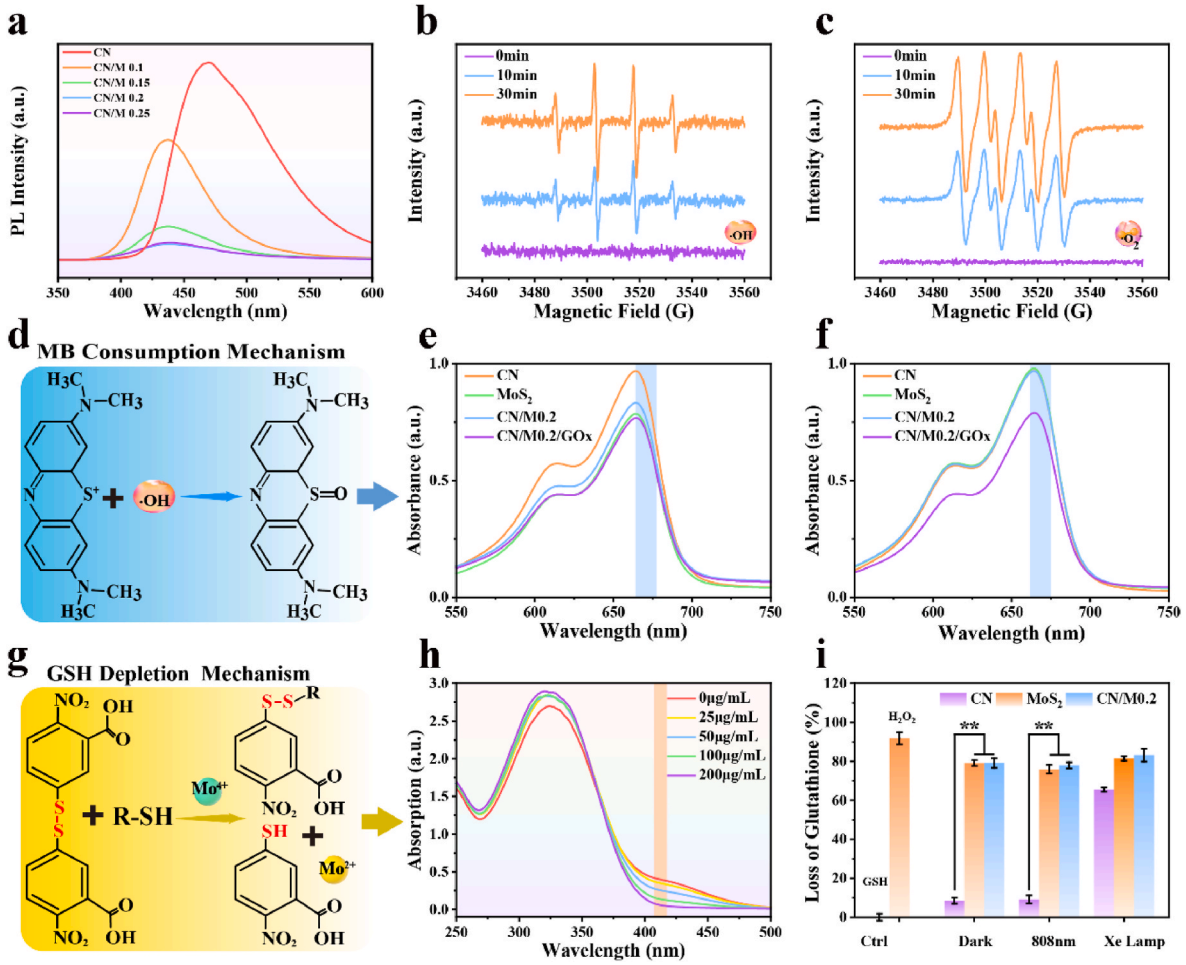

Fig. 5. (a) PL spectra of various samples; ESR spectra of (b, c) CN/M0.2 for the detection of ·OH and·O_2^- generated by DMPO under dual light; (d) MB consumption mechanism; (e) MB consumption of each sample in the presence of H_2O_2; (f) MB consumption of each sample in the presence of glucose; (g) GSH depletion mechanism; (h) GSH consumption of CN/M0.2 at different concentrations; (i) GSH exhaustion of each sample treated with different conditions. (* represents $p < 0.05$, ** represents $p < 0.01$).

$$\text{Glucose} + O_2 + H_2O \rightarrow \text{Gluconic acid} + H_2O_2 \quad (7)$$

Similarly, as shown in Fig. 5f, only the CN/M0.2/GOx group exhibits a decrease in the MB absorption peak, whereas the other groups show no degradation of MB. In the presence of glucose, GOx can produce H_2O_2 (Formula (7)), which is then catalytically yielded ·OH for enhancing the chemodynamic effect of CN/M0.2/GOx C-bio-HJs.

Glutathione (GSH), a tripeptide with a thiol group, has been proven to have antioxidant properties and become a well-known "self-defense system" in bacteria by oxidizing organic thiols (R–SH) to disulfides (R-S-S-R) *via* the mechanism described in Fig. 5g, which is a self-protective system in bacteria [59]. The oxidation of GSH was determined through Ellman's method, and the GSH consumption rate obeys positive linearity with the sample concentration, i.e. as the concentration of CN/M0.2 increases, the consumption of GSH increases significantly (Fig. 5h). Fig. 5i shows that both the CN/M0.2 and MoS_2 groups exhibit approximately 80% GSH consumption in the presence and absence of light, whereas the CN group exhibits comparable GSH consumption rate only under Xe lamp irradiation. This is due to the fact that Mo^{4+} in MoS_2 has glutathione peroxidase activity, which oxidizes glutathione to GSSG (Formula (8)) [17]. Therefore, the exhaustion of GSH in each group can be attributed to the oxidative damage of MoS_2.

$$Mo^{4+} + GSH \rightarrow Mo^{2+} + GSSG \quad (8)$$

Altogether, based on DFT calculations and previous results, the photothermal and photodynamic antibacterial mechanism of CN/M0.2/GOx C-bio-HJs is illustrated in Fig. 3f. Electrons in CN can absorb light energy to produce photogenerated electron-hole pairs. Due to the construction of CN/M/GOx C-bio-HJs, MoS_2 can promote the separation of CN photogenerated electron-hole pairs and inhibit their complexation by accelerating carrier transfer. Moreover, according to the above-described DFT calculations, from the electrostatic potential of the sample shown in Fig. 3e, also confirms that electrons transfer from MoS_2 to CN [43]. Under light irradiation, electrons are captured by O_2 generated from CN splitting water to produce ·O_2^-. GOx catalyzes the surrounding glucose to produce H_2O_2, and then MoS_2 further catalyzes H_2O_2 to produce ·OH. With the simultaneous absorption of photoelectron heat production by MoS_2, bacteria can be more sensitive to these photo-activated ROS, thus achieving serious antibacterial effects. The specific electron transfer process is shown in the following equations (9) (10):

$$e\ (MoS_2/CN) + O_2 \rightarrow \cdot O_2^- \quad (9)$$

$$e\ (MoS_2/CN) + H_2O_2 \rightarrow \cdot OH + OH^- \quad (10)$$

Then, it is necessary to state importantly here that g-C_3N_4, a material reported to separate water under white light with a band gap of 2.7 eV, can produce O_2, which facilitates the alleviation of deep hypoxia *in vivo* and thus enhances the PDT effect. Furthermore, MoS_2 has a high photothermal conversion efficiency under 808 nm laser, and the heat can not only render the bacteria to become more sensitive to ROS but can also further enhance the GOx cascade catalytic ability, so the photothermal-photodynamic synergistic antibacterial effect can be realized.

In addition, as mentioned earlier, GOx can oxidize glucose to produce H_2O_2, and MoS_2 exhibits peroxidase-like and Fenton-like reaction activities, which can achieve chemodynamic anti-bacterial effect *via* ·OH generation. Therefore, the CN/M0.2/GOx C-bio-HJs with dual light illumination exerts a triple synergistic antibacterial effect of PTT/PDT/CDT and have significant application potential in the field of antibacterial therapy.

3.5. *In vitro* antibacterial effect

The antibacterial performance of CN/M0.2/GOx C-bio-HJs was tested utilizing *S. aureus* and *E. coli* in this work. The spread plate results of *S. aureus* (Fig. 6a) reveal that CN has no significant antibacterial activity when cultured with bacteria for 10 min under dark or light conditions, compared with the control group; hence, it cannot produce sufficient ROS to kill bacteria. The results shown in Fig. 6a–b indicate that the anti-bacterial effect of MoS_2 has certainly improved under darkness (15.82 ± 9.18%), whereas it also increases to 43.15 ± 8.26% and 51.78 ± 5.69% under a single 808 nm laser and dual light irradiation, respectively. This result indicates that although a single PTT can play a role in killing bacteria, the anti-bacterial effect is far from ideal. Moreover, the antibacterial effect of MoS_2 against *S. aureus* does not have a significant difference between Xe lamp and dark condition. For CN/M0.2, the antibacterial effect, shown in Fig. 6b, is almost consistent with a mono MoS_2 in darkness. The antibacterial effect is significantly improved to 43.46 ± 3.56% and 32.71 ± 10.4% under the single irradiation of 808 nm laser and Xe lamp conditions, respectively, but not exceeding 50%. When the Xe lamp is combined with and 808 nm laser illumination, the antibacterial efficiency of CN/M0.2 is remarkably increased (> 95%). This is because CN can split water to produce more

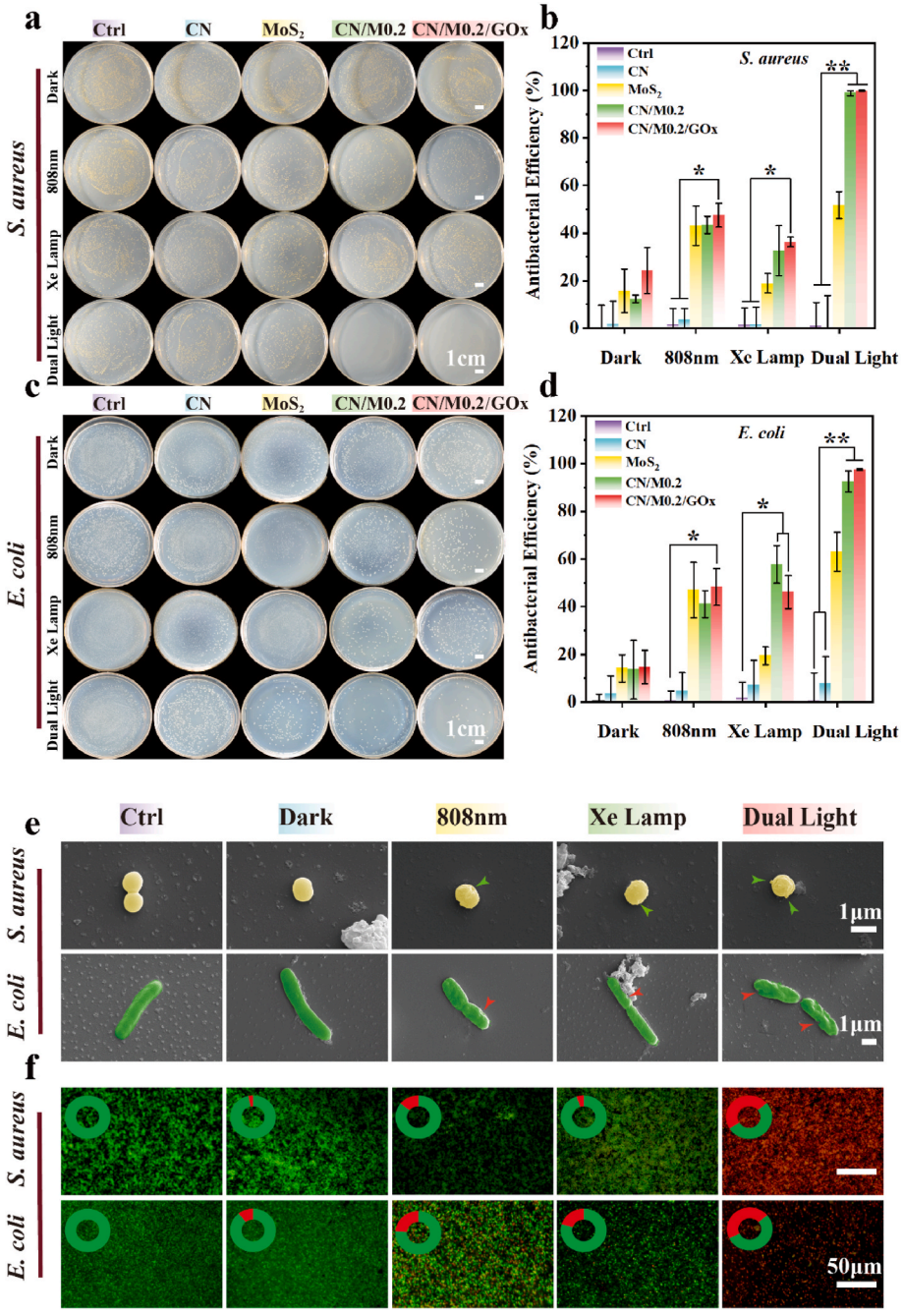

Fig. 6. *In vitro* antibacterial activity: Spread plate image showing (a) *S. aureus* and (b) *E. coli* eradication with different samples following treatment in the darkness or light for 10 min; The spread plate method was used to assess the antibacterial rates of (c) *S. aureus* and (d) *E. coli*; (e) SEM morphology and (f) Live/Dead staining of *S. aureus* and *E. coli* treated with CN/M0.2/GOx C-bio-HJs in the darkness or light for 10 min. Green and red arrows indicate disruption or wrinkling of the membrane (* represents $p < 0.05$, ** represents $p < 0.01$).

oxygen under Xe lamp irradiation, and then when exposure to the 808 nm laser, the local high temperature and large amounts of ROS produced through the PTT and PDT effects simultaneously, so the use of dual light causes a significant increase in the antibacterial rate [30]. In addition, once GOx is loaded, the antibacterial effect of CN/M0.2/GOx C-bio-HJs also increases by 24.31 ± 9.71% in darkness (Fig. 6b); this is because GOx can effectively consume glucose *via* catalytic oxidation and generate H_2O_2, whereas MoS_2 can catalyze the decomposition of H_2O_2 to produce ·OH, producing a chemodynamic effect, although not yet satisfactory. The antibacterial performance of CN/M0.2/GOx C-bio-HJs increases to 47.55 ± 5.01% under 808 nm laser, and it may achieve the synergistic antibacterial effect of CDT and PTT. In particular, its antibacterial performance is the largest, under dual light illumination because of the combined effect of PDT/PTT/CDT. Similarly, the trend of antibacterial effect against *E. coli* agrees with that against *S. aureus* (Fig. 6c). The CN/M0.2/GOx group has the smallest colony area after exposure to Xe lamp and 808 nm laser irradiation, with antibacterial performance displayed in Fig. 6d at 97.42 ± 0.31%, and that of CN/M at 92.53 ± 4.34%; while the other groups still show large colony area, confirming the superiority of synergistic antibacterial effect over the single modality.

To investigate the interaction between CN/M0.2/GOx C-bio-HJs and bacteria, we examined the bacterial membrane morphology and integrity after treatment with or without light and then observed it by SEM. The live bacterial membrane in both *S. aureus* and *E. coli* is smooth morphologically, whereas that of dead bacteria is shattered, as illustrated in Fig. 6e. The bacterial membrane is intact and has no wrinkles in the control group and the group treated under dark condition, illustrating that no damage has been made to the bacteria. Moreover, after treatment with Xe lamp or 808 nm laser, there are slight deformation and cytoplasmic leakage that are more deteriorating under 808 nm laser condition (indicated by green and red arrows, respectively). The membrane of *S. aureus* and *E. coli* exposed to dual light exhibits serious irreversible damage with unsmooth dimples and bulges (indicated by green and red arrows, respectively), further confirming the results of spread plate experiment.

The Live/Dead viability assay was also used to determine the antibacterial efficacy of the samples. Fig. 6f shows images of *S. aureus* and *E. coli* obtained from fluorescence staining analysis. Obviously, all the bacteria are stained with green fluorescence (representing alive), indicating that the negligible antibacterial activity of CN/M0.2/GOx C-bio-HJs under dark condition, with limited toxicity to the bacteria in a short period. Fewer bacteria are stained with red fluorescence (representing dead), whereas more bacteria exhibit green fluorescence in the single Xe lamp or 808 nm laser irradiation, indicating that most bacteria cannot be killed by singe PDT or PTT. In sharp contrast, after combined irradiation, the bacteria are almost entirely labeled with red fluorescence, suggesting that they are destroyed by the synergistic impact of CDT/PDT/PTT.

3.6. In vitro biocompatibility

We performed Live/Dead staining and CCK-8 assay to evaluate the biocompatibility of CN, MoS_2, CN/M0.2, and CN/M0.2/GOx. The Live/Dead staining results after culturing with L929 cells at 37 °C for 1 day are shown in Fig. S4a, Supporting Information. The MoS_2 group presents the fewest number of cells and the strongest red fluorescence, representing a lower cell survival assay than CN. Correspondingly, the CN/M0.2 and CN/M0.2/GOx groups exhibit little red fluorescence, with almost green fluorescence, indicating that good cytocompatibility. Moreover, the CCK-8 assay result (Fig. S4b, Supporting Information) shows that MoS_2 exhibits the worst cell viability after 1 day of cell culture, which may be explained by the fact that MoS_2 can consume glutathione and then induce oxidative stress in cells. However, the cell viability of CN/M0.2 and CN/M0.2/GOx is significantly potentiated, indicating that the CN and MoS_2 composite preparation into a heterojunction can improve their biocompatibility. When the incubation time is extended to 3 and 5 days, the cell activity in each group increased steadily, except for MoS_2. In short, at the cellular level, the CN/M0.2/GOx C-bio-HJs shows relatively good biocompatibility under long-term local treatment, and it will also be further verified in subsequent *in vivo* experiment.

3.7. In vivo antibacterial activity

To evaluate the antibacterial and cutaneous regeneration of CN/M0.2/GOx C-bio-HJs *in vivo*, we designed a diabetic mouse skin wound infection model on the dorsal of diabetic mice. Fig. 7a shows the entire *in vivo* experimental healing process. Briefly, the mouse-infected wound model was established followed by light treatment and histological analysis. The alterations in the wound area during the treatment are shown in Fig. 7b. Due to severe bacterial infection, the wound is in a state of inflammation and suppuration in the control group during the entire repair process, and there are numerous secretions and pus visible with the naked eye. The wound is also not completely healed, indicating that self-immunity is far from sufficient to repair the infected skin. Similarly, both the single light and dark groups show conspicuous crusts but incomplete recovery. In contrast, in the dual light group, the secretions and pus in the wound are significantly reduced at 1 day and the wound basically was healed at 7 days, with no suppuration and crusting. This result indicates that CN/M0.2/GOx C-bio-HJs can effectively kill bacteria and promote cutaneous regeneration under dual light. Fig. 7e shows the corresponding quantitative data throughout the wound healing process, confirming that the wound healing effect is the best at dual light conditions. Although the wound healing effects of light and dark groups are superior to that of the control group, the difference is not statistically significant after 5 and 7 days. Based on the body weight curve for 7 days (Fig. 7f), the trend in each group is essentially similar. The body weight shows less variation during the entire treatment process, revealing almost no side effects during treatment. The infrared images shown in Fig. 7c indicate that there is little change in wound temperature in mice either under dark conditions or under Xe lamp irradiation, suggesting that the 808 nm laser trigger is required to exert the photothermal properties of C-bio-HJs. The wound temperature in the CN/M0.2/GOx group increases considerably under 808 nm laser and dual light, reaching approximately 48 °C and 51 °C, respectively, within 5 min and then stabilized. The corresponding temperature change curve is displayed in Fig. S5a, Supporting Information. As we previously mentioned, although the bacteria cannot be killed directly in a short period at this temperature, it can augment the sensitivity of the bacteria to ROS stimulation, thus enhancing the antibacterial effect.

To further confirm the antibacterial properties of CN/M0.2/GOx C-bio-HJs *in vivo*, we extracted wound tissue fluid after 10 min of light treatment and incubated it in beef paste peptone medium for 24 h before performing plate coating experiments. The spread plate results are displayed in Fig. 7d, which show only a few bacterial colonies in the dual light treated group, with an antibacterial efficacy of 94.05 ± 1.87% (Fig. 7g). The colony area decreases in the dark, Xe lamp and 808 nm laser groups sequentially compared with the PBS group, and the corresponding antibacterial rates are 6.38 ± 4.97%, 22.38 ± 8.26%, and 47.13 ± 4.16%, respectively. These results are also consistent with the *in vitro* antibacterial parts.

We collected wound tissue for the histological investigation to analyze the level of bacterial infection and inflammation in the skin tissue. As shown by the H&E staining results in Fig. 8a, there is obvious acute inflammation and neutrophil infiltration, presenting a typical feature of soft tissue infection in the PBS and dark groups, with orange lines outlining the state of the epithelial layer. Under Xe lamp or 808 nm laser irradiation separately, the inflammatory response is milder, and the number of inflammatory cells is also reduced to a certain extent, but there is still a large subcutaneous distance, which suggests that the skin is healed incompletely. However, improvement can be found under dual light, with all mice wounds showing the best recovery with no scar.

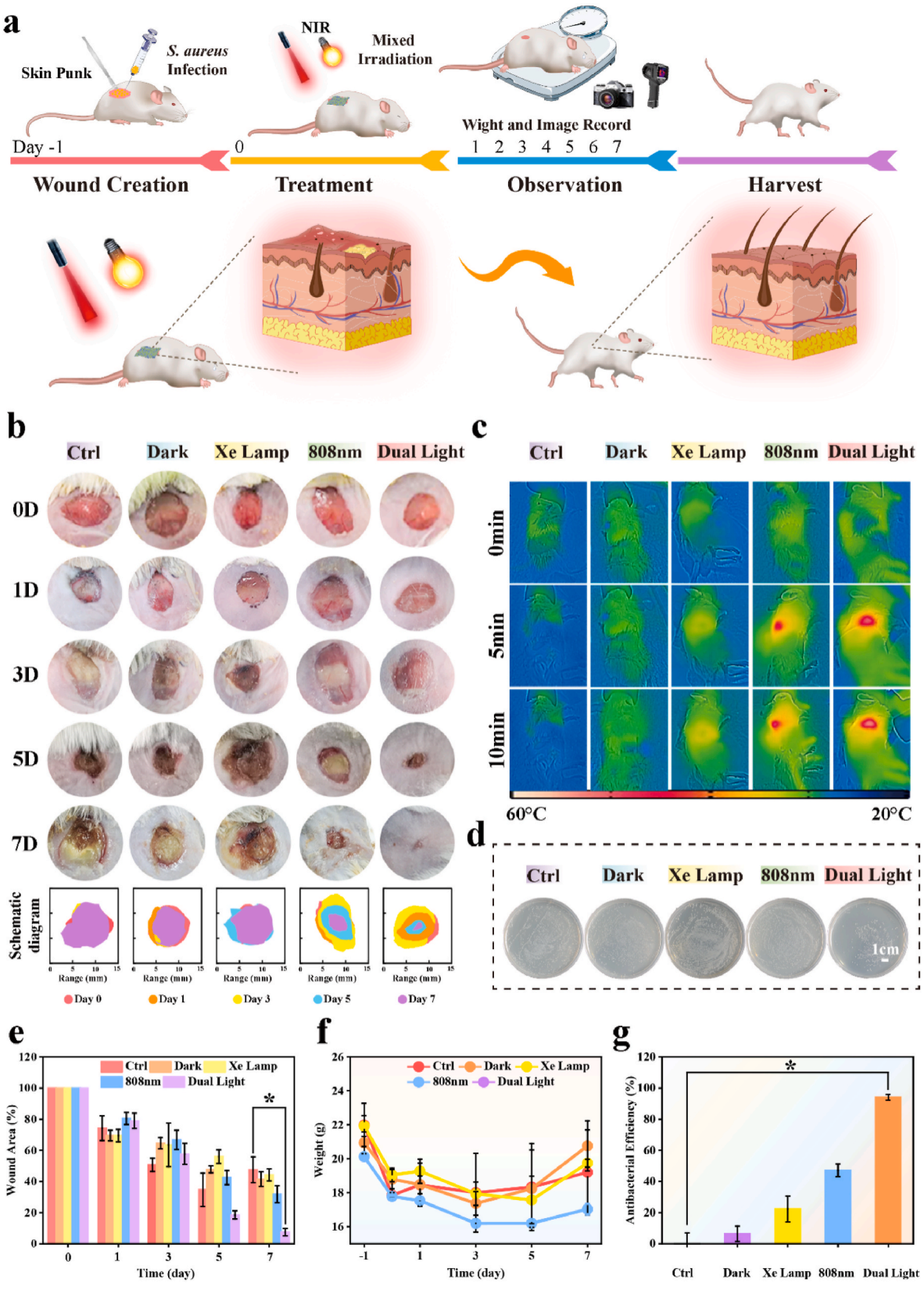

Fig. 7. Evaluation of antibacterial activity *in vivo*. (a) The following therapies are depicted in a schematic diagram of the diabetic mouse with infected wound; (b) Photographs of changes in the wound area of mice during treatment; (c) Infrared images of each group after 10 min of illumination; (d) *In vivo* spread plate photos following dark treatment or irradiation with NIR light after 10 min; (e) Quantitative data of the wound area of mice during treatment; (f) Body weight of mice during treatment; (g) *In vivo* antibacterial efficacy following dark therapy or irradiation with NIR light for 10 min (* represents $p < 0.05$, ** represents $p < 0.01$).

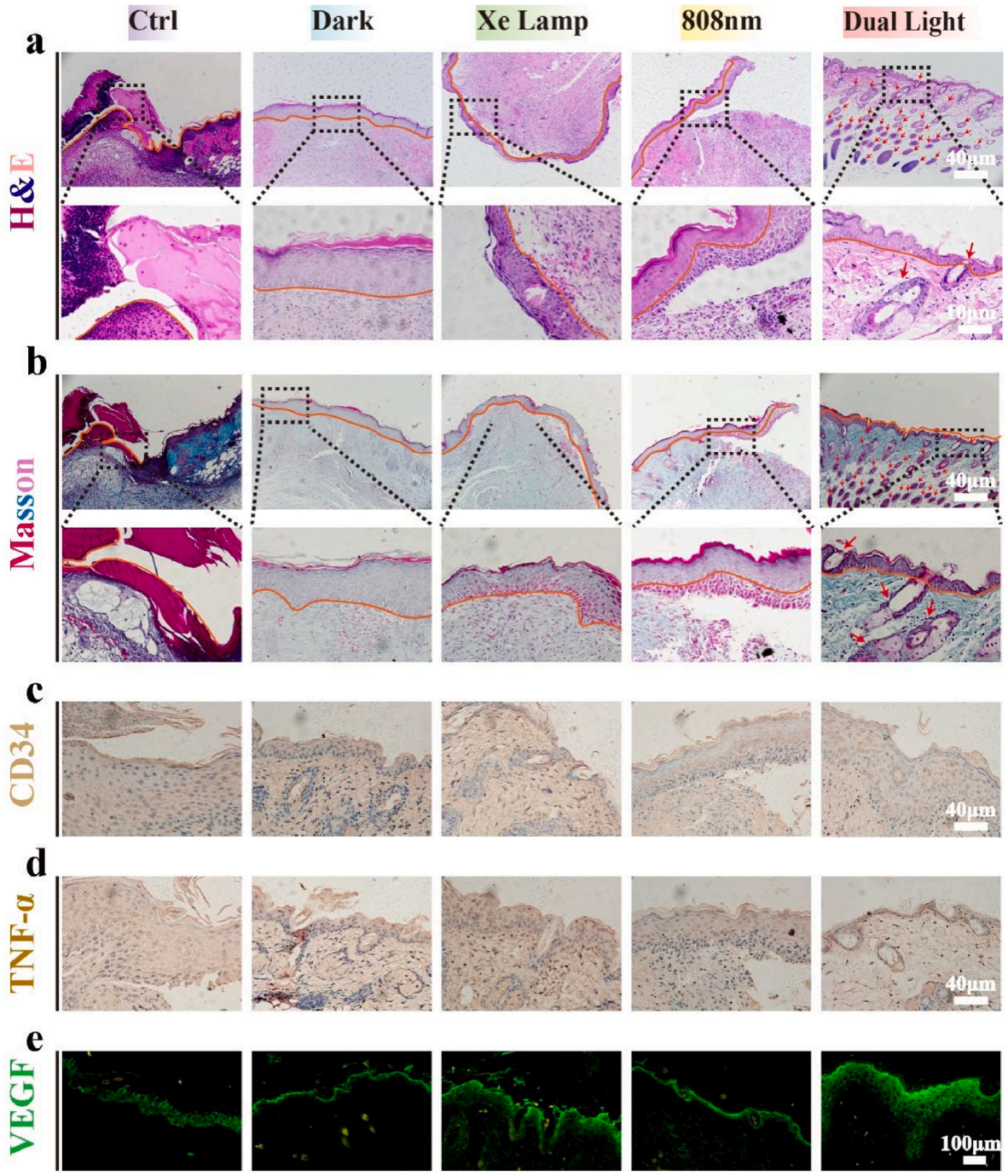

Fig. 8. Histological analysis of wounds after a 7-day treatment with CN/M0.2/GOx C-bio-HJs (a) H&E staining images; (b) Masson's trichrome images; (c) CD34 staining images; (d) TNF-α staining images; and (e) VEGF fluorescence images of wound skin tissue.

Furthermore, a complete epidermis is formed generally with a thickness of approximately 100 μm, and new blood vessels and hair follicles marked by permanent red asterisks can be observed in the dual light group (Fig. 8a). There are no obvious inflammation and infection, confirming the antibacterial results of the above-described CN/M0.2/GOx C-bio-HJs *in vivo* experiments. Masson's trichrome staining was used to confirm the development of collagen fibers to better understand tissue regeneration around the lesion. As shown in Fig. 8b, the collagen fibers of the wound are arranged continuously in the dual light irradiation group, with several new hair follicles (red arrows), whereas the other groups show disordered and sparse collagen fibers in the inflammatory infiltrated areas. In addition, Giemsa staining was used to further characterize the bacteria in the tissues. As can be seen in Fig. S6, Supporting Information, the PBS and dark groups show bacteria (yellow arrows), while a small amount is also present in the single light treatment group and almost no bacteria in the dual light treatment group. Hence, the implementation of CN/M0.2/GOx C-bio-HJs can effectively kill bacteria while also encouraging wound healing and regeneration.

The role of various cell-secreted growth factors, such as CD34 protein molecule, tumor necrosis factor-α (TNF-α), and vascular endothelial growth factor (VEGF), all of which have a vital function in wound healing, was further explored [60]. In fact, CD34 is expressed on a major subset of stem cells known as fibrocytes and has recently been investigated in clinical trials to hasten wound healing, predominantly due to its

potential to enhance angiogenic activity [61]. We observe more CD34 expression in diabetic mice in the wound healing process (day 7), with the strongest CD34 expression under exposure to dual light conditions (Fig. 8c), indicating the formation of microvessels. TNF-α is an inflammatory cytokine whose production prolongs the healing time of chronic wounds in an inflammatory environment, which can be detrimental to wound recovery in diabetic patients [62]. As shown in Fig. 8d, TNF-α levels are reduced with the illumination of Xe lamp and 808 nm laser continuously, indicating that CN/M0.2/GOx C-bio-HJs exerts a prominent beneficial effect on wound healing. VEGF is also well known to play an essential role in tissue repair, which contributes to inflammatory processes. VEGF may accelerate wound closure and promote wound healing, primarily by stimulating the production of angiogenesis. Moreover, wound healing in patients with diabetes is generally delayed, which is commonly characterized by a lower local VEGF production [64, 63]. Therefore, enhancing the expression levels of VEGF could be employed topically to accelerate wound healing in diabetic patients. As shown in Fig. 8e, the fluorescence intensity is obviously enhanced in the epidermis under the dual light illumination, indicating an augmentation in VEGF expression, which facilitates wound healing. Also, the corresponding quantitative data, in Fig. S5b, Supporting Information, directly shows the enhancement of fluorescence intensity under dual light treatment.

To test whether CN/M0.2/GOx C-bio-HJs could cause severe *in vivo* toxicity, we conducted hematological and pathological examinations in mice. After 7 days of different light treatments, the analysis result, shown as a heatmap (Fig. S7, Supporting Information), the number of white blood cells (RBC) and neutrophils (NEUT) in the dual light illumination group is significantly lower than that of the other groups, indicating that the wound inflammation became less. CN/M0.2/GOx C-bio-HJs could efficiently protect the skin from inflammation and infection by rapidly killing bacteria in the presence of dual light. For the rest of blood indicators like red blood cells (RBC), hemoglobin (HGB), red blood cell ratio (HCT), and platelet count (PLT), none of the groups of mice showed significant differences, which indicates that CN/M0.2/GOx C-bio-HJs can not cause toxicity of normal cells *in vivo*. Finally, the main organs, including the heart, liver, spleen, lung, and kidney, were taken and stained with H&E to validate the above-mentioned findings. As shown in Fig. S8, Supporting Information, no alteration in cellular morphology and shape is observed after 7 days, and no obvious organ damage or abnormality is evident, indicating a favorable biosafety profile. At present, the application and research of CN based materials in the field of biomedical engineering are in their infancy and exploration stage, and there is still a broad space for exploration and development. The future development and research of such antibacterial materials will need to combine various approaches and strategies to improve the biocompatibility of the materials and promote wound healing, and to obtain a therapeutic system with both rapid antimicrobial and tissue repair functions.

4. Conclusion

In summary, we successfully developed the CN/M/GOx C-bio-HJs with a combined therapeutic effect for cutaneous healing in the diabetic microenvironment. The C-bio-HJs facilitates the separation of the photogenerated electron-hole pairs of CN, which considerably boosted the efficiency of ROS generation. GOx in C-bio-HJs could consume a high level of glucose in diabetic wounds, leading to the generation of large amounts of H_2O_2. Furthermore, C-bio-HJs not only have outstanding water splitting capability to O_2 generation for augmented photodynamic effect, but they can also catalyze the GOx-generated H_2O_2 into highly reactive bactericidal hydroxyl radicals *via* the Fenton-like reaction of MoS_2, which can lead to bacterial death. The CN/M0.2/GOx C-bio-HJs have exceptional synergistic antibacterial activity and good biosafety, according to *in vitro* and *in vivo* studies. Such C-bio-HJs can be successfully combined with PDT, PTT, and CDT to kill pathogens and combat bacterial infections. This work offers a new avenue for cascaded nano-heterojunction catalysts providing for diabetes therapy.

Ethics approval and consent to participate

All the animals were acclimated under standard laboratory conditions (ventilated room, 25 ± 1 °C, 60 ± 5% humidity, 12 h light/dark cycle) and had free access to standard water and food (SYXK-2013-026). All procedures were conducted in accordance with the "Guiding Principles in the Care and Use of Animals" (China) and were approved by **the Medical Ethics Committee of Sichuan University with the following reference number: No.2021605A.**

CRediT authorship contribution statement

Yi Deng: Writing – review & editing, Funding acquisition, Project administration. **Xumei Ouyang:** Writing – original draft. **Jiyu Sun:** Software. **Xiuyuan Shi:** Visualization, Resources. **Yunfei Li:** Supervision. **Yau Kei Chan:** Formal analysis. **Weizhong Yang:** Conceptualization, Methodology, Funding acquisition. **Shaojun Peng:** Data curation, Validation, Writing – review & editing, Funding acquisition.

Declaration of interests

The authors declare that they have no known competing financial interests or personal relationships that could have appeared to influence the work reported in this paper.

Acknowledgments

This work is jointly funded by the National Natural Science Foundation of China (81961160736, 81801848, 82172073, 8217070298), Natural Science Foundation of Sichuan Province (2022NSFSC0361), Sichuan Science and Technology Program (2021YJ0049), Chengdu International Science and Technology Cooperation Foundation (2020-GH03-00005-HZ, 2017-GH02-00025-HZ), State Key Laboratory of Polymer Materials Engineering (sklpme2019-2-05), Young Elite Scientist Sponsorship Program by CAST, Sichuan University-Luzhou City Special Funding for Strategic Cooperation (2020CDLZ-5). The authors also thank Hui Wang, Daichuan Ma, Daibing Luo (Analytical & Testing Center, Sichuan University) for their help in SEM, XRD and UV–vis characterization. We would like to thank Wen Tian and Yanping Huang from Center of Engineering Experimental Teaching, School of Chemical Engineering, Sichuan University for the help of FTIR spectrometer and SEM measurements.

Appendix A. Supplementary data

Supplementary data to this article can be found online at https://doi.org/10.1016/j.bioactmat.2022.07.003.

References

[1] V. Falanga, Wound healing and its impairment in the diabetic foot, Lancet 366 (2005) 1736–1743.
[2] D.G. Armstrong, A.J.M. Boulton, S.A. Bus, Diabetic foot ulcers and their recurrence, N. Engl. J. Med. 376 (2017) 2367–2375.
[3] G.C. Gurtner, S. Werner, Y. Barrandon, M.T. Longaker, Wound repair and regeneration, Nature 453 (2008) 314–321.
[4] T. Tuomi, N. Santoro, S. Caprio, M. Cai, J. Weng, L. Groop, The many faces of diabetes: a disease with increasing heterogeneity, Lancet 383 (2014) 1084–1094.
[5] C.A. Thaiss, M. Levy, I. Grosheva, D. Zheng, E. Soffer, E. Blacher, S. Braverman, A. C. Tengeler, O. Barak, M. Elazar, R. Ben-Zeev, D. Lehavi-Regev, M.N. Katz, M. Pevsner-Fischer, A. Gertler, Z. Halpern, A. Harmelin, S. Aamar, P. Serradas, A. Grosfeld, H. Shapiro, B. Geiger, E. Elinav, Hyperglycemia drives intestinal barrier dysfunction and risk for enteric infection, Science 359 (2018) 1376–1383.
[6] P.Z. Zimmet, D.J. Magliano, W.H. Herman, J.E. Shaw, Diabetes: a 21st century challenge, Lancet Diabetes Endocrinol. 2 (2014) 56–64.
[7] K.E. Jones, N.G. Patel, M.A. Levy, A. Storeygard, D. Balk, J.L. Gittleman, P. Daszak, Global trends in emerging infectious diseases, Nature 451 (2008) 990–993.

[8] L. Diacovich, J.P. Gorvel, Bacterial manipulation of innate immunity to promote infection, Nat. Rev. Microbiol. 8 (2010) 117–128.
[9] A. Gupta, S. Mumtaz, C.H. Li, I. Hussain, V.M. Rotello, Combatting antibiotic-resistant bacteria using nanomaterials, Chem. Soc. Rev. 48 (2019) 415–427.
[10] J.M.V. Makabenta, A. Nabawy, C.H. Li, S. Schmidt-Malan, R. Patel, V.M. Rotello, Nanomaterial-based therapeutics for antibiotic-resistant bacterial infections, Nat. Rev. Microbiol. 19 (2021) 23–36.
[11] C. Cao, W. Ge, J. Yin, D. Yang, W. Wang, X. Song, Y. Hu, J. Yin, X. Dong, Mesoporous silica supported silver-bismuth nanoparticles as photothermal agents for skin infection synergistic antibacterial therapy, Small 16 (2020), e2000436.
[12] C. Liu, X. Xu, W. Cui, H. Zhang, Metal-organic framework (MOF)-based biomaterials in bone tissue engineering, Eng. Regen. 2 (2021) 105–108.
[13] Q. Sun, F. He, H. Bi, Z. Wang, C. Sun, C. Li, J. Xu, D. Yang, X. Wang, S. Gai, P. Yang, An intelligent nanoplatform for simultaneously controlled chemo-, photothermal, and photodynamic therapies mediated by a single NIR light, Chem. Eng. J. 362 (2019) 679–691.
[14] X. Kong, X. Liu, Y. Zheng, P. Chu, Y. Zhang, S. Wu, Graphitic carbon nitride-based materials for photocatalytic antibacterial application, Math. Sci. Eng. R 145 (2021), 100610.
[15] F. Chen, Y. Luo, X. Liu, Y. Zheng, Y. Han, D. Yang, S. Wu, 2D molybdenum sulfide-based materials for photo-excited antibacterial application, Adv. Healthc. Mater. (2022), 2200360.
[16] H.P. Lee, A.K. Gaharwar, Light-responsive inorganic biomaterials for biomedical applications, Adv. Sci. 7 (2020), 2000863.
[17] M. Li, L. Li, K. Su, X. Liu, T. Zhang, Y. Liang, D. Jing, X. Yang, D. Zheng, Z. Cui, Z. Li, S. Zhu, K.W.K. Yeung, Y. Zheng, X. Wang, S. Wu, Highly effective and noninvasive near-infrared eradication of a staphylococcus aureus biofilm on implants by a photoresponsive coating within 20 min, Adv. Sci. 6 (2019), 1900599.
[18] X. Gao, M. Wei, D. Ma, X. Yang, Y. Zhang, X. Zhou, L. Li, Y. Deng, W. Yang, Engineering of a hollow-structured $Cu_{2-X}S$ nano-homojunction platform for near infrared-triggered infected wound healing and cancer therapy, Adv. Funct. Mater. 31 (2021), 2106700.
[19] H. Sun, Q. Zhang, J. Li, S. Peng, X. Wang, R. Cai, Near-infrared photoactivated nanomedicines for photothermal synergistic cancer therapy, Nano Today 37 (2021).
[20] S.S. Lucky, K.C. Soo, Y. Zhang, Nanoparticles in photodynamic therapy, Chem. Rev. 115 (2015) 1990–2042.
[21] J. Huo, Q. Jia, H. Huang, J. Zhang, P. Li, X. Dong, W. Huang, Emerging photothermal-derived multimodal synergistic therapy in combating bacterial infections, Chem. Soc. Rev. 50 (2021) 8762–8789.
[22] X. Hu, L. Chu, X. Dong, G. Chen, T. Tang, D. Chen, X. He, H. Tian, Multivalent glycosheets for double light–driven therapy of multidrug-resistant bacteria on wounds, Adv. Funct. Mater. 29 (2019), 1806986.
[23] Z. Zhang, Y. Wang, W. Teng, X. Zhou, Y. Ye, H. Zhou, H. Sun, F. Wang, A. Liu, P. Lin, W. Cui, X. Yu, Y. Wu, Z. Ye, An orthobiologics-free strategy for synergistic photocatalytic antibacterial and osseointegration, Biomaterials 274 (2021), 120853.
[24] W. Guo, Z. Qiu, C. Guo, D. Ding, T. Li, F. Wang, J. Sun, N. Zheng, S. Liu, Multifunctional theranostic agent of $Cu_2(OH)PO_4$ quantum dots for photoacoustic image-guided photothermal/photodynamic combination cancer therapy, ACS Appl. Mater. Interfaces 9 (2017) 9348–9358.
[25] M. Liu, D. He, T. Yang, W. Liu, L. Mao, Y. Zhu, J. Wu, G. Luo, J. Deng, An efficient antimicrobial depot for infectious site-targeted chemo-photothermal therapy, J. Nanobiotechnol. 16 (2018) 23.
[26] Y. Xu, X. Liu, Y. Zheng, C. Li, K.W.K. Yeung, Z. Cui, Y.Q. Liang, Z. Li, S. Zhu, S. Wu, Ag_3PO_4 decorated black urchin-like defective TiO_2 for rapid and long-term bacteria-killing under visible light, Bioact. Mater. 6 (2021) 1575–1587.
[27] S. Wei, Y. Qiao, Z. Wu, X. Liu, Y. Li, Z. Cui, C. Li, Y. Zheng, Y. Liang, Z. Li, S. Zhu, H. Wang, X. Wang, R. Che, S. Wu, Na^+ inserted metal-organic framework for rapid therapy of bacteria-infected osteomyelitis through microwave strengthened fenton reaction and thermal effects, Nano Today 37 (2021), 101090.
[28] D. Han, Y. Li, X. Liu, K.W.K. Yeung, Y. Zheng, Z. Cui, Y. Liang, Z. Li, S. Zhu, X. Wang, S. Wu, Photothermy-strengthened photocatalytic activity of polydopamine-modified metal-organic frameworks for rapid therapy of bacteria-infected wounds, J. Mater. Sci. Technol. 62 (2021) 83–95.
[29] C. Fasciani, M.J. Silvero, M.A. Anghel, G.A. Arguello, M.C. Becerra, J.C. Scaiano, Aspartame-stabilized gold-silver bimetallic biocompatible nanostructures with plasmonic photothermal properties, antibacterial activity, and long-term stability, J. Am. Chem. Soc. 136 (2014) 17394–17397.
[30] J. Zhang, X. Gao, D. Ma, S. He, B. Du, W. Yang, K. Xie, L. Xie, Y. Deng, Copper ferrite heterojunction coatings empower polyetheretherketone implant with multi-modal bactericidal functions and boosted osteogenicity through synergistic photo/fenton-therapy, Chem. Eng. J. 442 (2021), 130094.
[31] S. Cao, J. Low, J. Yu, M. Jaroniec, Polymeric photocatalysts based on graphitic carbon nitride, Adv. Mater. 27 (2015) 2150–2176.
[32] X. Zhang, X. Yuan, L. Jiang, J. Zhang, H. Yu, W. Hou, G. Zeng, Powerful combination of 2D g-C_3N_4 and 2D nanomaterials for photocatalysis: recent advances, Chem. Eng. J. 390 (2020), 124475.
[33] H. Yu, Y. Cheng, C. Wen, Y.Q. Sun, X. Yin, Triple cascade nanocatalyst with laser-activatable O_2 supply and photothermal enhancement for effective catalytic therapy against hypoxic tumor, Biomaterials 280 (2022), 121308.
[34] D. Zheng, B. Li, C. Li, J. Fan, Q. Lei, C. Li, Z. Xu, X. Zhang, Carbon-dot-decorated carbon nitride nanoparticles for enhanced photodynamic therapy against hypoxic tumor via water splitting, ACS Nano 10 (2016) 8715–8722.
[35] W. Ong, L. Tan, Y. Ng, S. Yong, S. Chai, Graphitic carbon nitride (g-C_3N_4)-based photocatalysts for artificial photosynthesis and environmental remediation: are we a step closer to achieving sustainability? Chem. Rev. 116 (2016) 7159–7329.
[36] Y. Hou, Z. Wen, S. Cui, X. Guo, J. Chen, Constructing 2D porous graphitic C_3N_4 nanosheets/nitrogen-doped graphene/layered MoS_2 ternary nanojunction with enhanced photoelectrochemical activity, Adv. Mater. 25 (2013) 6291–6297.
[37] P. Xia, S. Cao, B. Zhu, M. Liu, M. Shi, J. Yu, Y. Zhang, Designing a 0D/2D S-scheme heterojunction over polymeric carbon nitride for visible-light photocatalytic inactivation of bacteria, Angew. Chem. Int. Ed. 59 (2020) 5218–5225.
[38] H. Ding, D. Han, Y. Han, Y. Liang, X. Liu, Z. Li, S. Zhu, S. Wu, Visible light responsive CuS/protonated g-C_3N_4 heterostructure for rapid sterilization, J. Hazard Mater. 393 (2020), 122423.
[39] W. Shi, C. Liu, M. Li, X. Lin, F. Guo, J. Shi, Fabrication of ternary $Ag_3PO_4/Co_3(PO_4)(2)/g$-C_3N_4 heterostructure with following Type II and Z-Scheme dual pathways for enhanced visible-light photocatalytic activity, J. Hazard Mater. 389 (2020), 121907.
[40] Z. Yang, X. Fu, D. Ma, Y. Wang, L. Peng, J. Shi, J. Sun, X. Gan, Y. Deng, W. Yang, Growth factor-decorated Ti_3C_2 MXene/MoS_2 2D bio-heterojunctions with quad-channel photonic disinfection for effective regeneration of bacteria-invaded cutaneous tissue, Small 17 (2021), e2103993.
[41] Y. Li, R. Fu, Z. Duan, C. Zhu, D. Fan, Construction of multifunctional hydrogel based on the tannic acid-metal coating decorated MoS_2 dual nanozyme for bacteria-infected wound healing, Bioact. Mater. 9 (2022) 461–474.
[42] F. Wei, X. Cui, Z. Wang, C. Dong, J. Li, X. Han, Recoverable peroxidase-like Fe_3O_4@MoS_2-Ag nanozyme with enhanced antibacterial ability, Chem. Eng. J. 408 (2021), 127240.
[43] L. Ye, D. Wang, S. Chen, Fabrication and enhanced photoelectrochemical performance of MoS(2)/S-doped g-C(3)N(4) heterojunction film, ACS Appl. Mater. Interfaces 8 (2016) 5280–5289.
[44] M.N. Xavier, M.G. Winter, A.M. Spees, A.B. den Hartigh, K. Nguyen, C.M. Roux, T. M. Silva, V.L. Atluri, T. Kerrinnes, A.M. Keestra, D.M. Monack, P.A. Luciw, R. A. Eigenheer, A.J. Baumler, R.L. Santos, R.M. Tsolis, PPARgamma-mediated increase in glucose availability sustains chronic Brucella abortus infection in alternatively activated macrophages, Cell Host Microbe 14 (2013) 159–170.
[45] H. Ma, Q. Yu, Y. Qu, Y. Zhu, C. Wu, Manganese silicate nanospheres-incorporated hydrogels starvation therapy and tissue regeneration, Bioact. Mater. 6 (2021) 4558–4567.
[46] J. Wang, L. Yao, E. Hu, Y. Cui, D. Yang, G. Qian, MnO_2 decorated ZIF-8@GOx for synergistic chemodynamic and starvation therapy of cancer, J. Solid State Chem. 298 (2021), 122102.
[47] L. Zhang, S. Wan, C. Li, L. Xu, H. Cheng, X. Zhang, An adenosine triphosphate-responsive autocatalytic fenton nanoparticle for tumor ablation with self-supplied H_2O_2 and acceleration of Fe(III)/Fe(II) conversion, Nano Lett. 18 (2018) 7609–7618.
[48] M. Wang, X. Zhou, Y. Li, Y. Dong, J. Meng, S. Zhang, L. Xia, Z. He, L. Ren, Z. Chen, X. Zhang, Triple-synergistic MOF-nanozyme for efficient antibacterial treatment, Bioact. Mater. 17 (2022) 289–299.
[49] H. Yu, R. Shi, Y. Zhao, T. Bian, Y. Zhao, C. Zhou, G.I.N. Waterhouse, L. Wu, C. Tung, T. Zhang, Alkali-assisted synthesis of nitrogen deficient graphitic carbon nitride with tunable band structures for efficient visible-light-driven hydrogen evolution, Adv. Mater. 29 (2017), 1605148.
[50] X. Zhou, Z. Wang, Y. Chan, Y. Yang, Z. Jiao, L. Li, J. Li, K. Liang, Y. Deng, Infection micromilieu-activated nanocatalytic membrane for orchestrating rapid sterilization and stalled chronic wound regeneration, Adv. Funct. Mater. 32 (2022), 2109469.
[51] P. Niu, L. Zhang, G. Liu, H. Cheng, Graphene-like carbon nitride nanosheets for improved photocatalytic activities, Adv. Funct. Mater. 22 (2012) 4763–4770.
[52] W. Fu, H. He, Z. Zhang, C. Wu, X. Wang, H. Wang, Q. Zeng, L. Sun, X. Wang, J. Zhou, Q. Fu, P. Yu, Z. Shen, C. Jin, B.I. Yakobson, Z. Liu, Strong interfacial coupling of MoS_2/g-C_3N_4 van de Waals solids for highly active water reduction, Nano Energy 27 (2016) 44–50.
[53] J. Zheng, X. Yan, Z. Lu, H. Qiu, G. Xu, Z. Xu, W. Peng, X. Pan, K. Liu, L. Jiao, High-mobility multilayered MoS_2 flakes with low contact resistance grown by chemical vapor deposition, Adv. Mater. 29 (2017), 1604540.
[54] X. Liu, Z. Yan, Y. Zhang, Z. Liu, Y. Sun, J. Ren, X. Qu, Two-dimensional metal-organic framework/enzyme hybrid nanocatalyst as a benign and self-activated cascade reagent for *in vivo* wound healing, ACS Nano 13 (2019) 5222–5230.
[55] H. Yang, R.M. Villani, H. Wang, M.J. Simpson, M.S. Roberts, M. Tang, X. Liang, The role of cellular reactive oxygen species in cancer chemotherapy, J. Exp. Clin. Cancer Res. 37 (2018) 266.
[56] A. Sattar, U. Moazzam, A.I. Bashir, A. Reza, H. Latif, A. Usman, R.J. Amjad, A. Mubshrah, A. Nasir, Proposal of graphene band-gap enhancement via heterostructure of graphene with boron nitride in vertical stacking scheme, Nanotechnology 32 (2021), 225705.
[57] A.J. Cohen, P. Mori-Sanchez, W.T. Yang, Insights into current limitations of density functional theory, Science 321 (2008) 792–794.
[58] L. Lin, J. Song, L. Song, K. Ke, Y. Liu, Z. Zhou, Z. Shen, J. Li, Z. Yang, W. Tang, G. Niu, H. Yang, X. Chen, Simultaneous fenton-like ion delivery and glutathione depletion by MnO_2-based nanoagent to enhance chemodynamic therapy, Angew. Chem. Int. Ed. 57 (2018) 4902–4906.
[59] H. Kawagishi, T. Finkel, Unraveling the truth about antioxidants: ROS and disease: finding the right balance, Nat. Med. 20 (2014) 711–713.
[60] P. Rousselle, F. Braye, G. Dayan, Re-epithelialization of adult skin wounds: cellular mechanisms and therapeutic strategies, Adv. Drug Deliv. Rev. 146 (2019) 344–365.
[61] J.S. Duffield, M. Lupher, V.J. Thannickal, T.A. Wynn, Host responses in tissue repair and fibrosis, Annu. Rev. Pathol. 8 (2013) 241–276.

[62] D.L. Anders, A piece of my mind, Risky business, JAMA. 260 (1988) 3184.
[63] J. Ishihara, A. Ishihara, R.D. Starke, C.R. Peghaire, K.E. Smith, T.A.J. McKinnon, Y. Tabata, K. Sasaki, M.J.V. White, K. Fukunaga, M.A. Laffan, M.P. Lutolf, A. M. Randi, J.A. Hubbell, The heparin binding domain of von Willebrand factor binds to growth factors and promotes angiogenesis in wound healing, Blood 133 (2019) 2559–2569.
[64] S. Korntner, C. Lehner, R. Gehwolf, A. Wagner, M. Grutz, N. Kunkel, H. Tempfer, A. Traweger, Limiting angiogenesis to modulate scar formation, Adv. Drug Deliv. Rev. 146 (2019) 170–189.